CFD Simulation of an Aerosol Mixing Chamber

Andrea Giordano
Master Program in Mechanical Engineering

Master's Thesis

Supervisors:
Dr. Stefan Horender, METAS
Dr. Mark Sawley, EPFL

August 27, 2020

Abstract

In the last years, the correlation between air pollution and health issues related to respiratory, cardiovascular and digestive systems has become evident. Today, urban aerosols raise the interest of both scientific community and public opinion. METAS, the Swiss Federal Institute of Metrology, takes part in AeroTox, a European Union's research project involving the development of a reference aerosol calibration infrastructure - a so-called *mixing chamber*. In this chamber, pure air and particles are injected on top and the resulting aerosol is sampled at the bottom. The quality of this aerosol is assessed according to its concentration homogeneity: the purpose of this master's project is to improve it.
In addition, two research questions were addressed. *How much can the mixing chamber dimensions be reduced without affecting the concentration homogeneity?* Dimensions are crucial because the mixing chamber must be transportable. Also, *how much can the flow rates be reduced without affecting the concentration homogeneity?*
Computational Fluid Dynamics (CFD) simulations and experiments were employed. Numerical simulations were performed in COMSOL Multiphysics, implementing a particle tracing and a diluted species model. This allowed to investigate the structure of the flow and the involved *mixing mechanisms*: diffusion, convection and turbulent dispersion. However, only the diluted species model was successful. The simulated concentration at the outlet is perfectly homogeneous. Experiments were carried out using two particle size distributions: $NaCl$ (size peak at 80 nm) and Polystyrene Latex (PSL, size peak at 900 nm). Empirical data validate simulations and show a concentration homogeneity within 5%. Furthermore, uncertainty on the measurements is of 4.24%: the simulated concentration homogeneity thus lies within the uncertainty of the experimental findings. Moreover, experiments show that salt particles reach a higher concentration homogeneity than PSL particles. Finally, in case of salt particles, experiments prove that the flow rates can be halved and even equalized and the length of the mixing chamber can be reduced to 50% without drastically affecting the concentration homogeneity.

Acknowledgements

This master's thesis has received funding from the EMPIR programme within the project 18HLT02 AeroTox co-financed by the Participating States and from the European Union's Horizon 2020 research and innovation programme.

Before starting, I would like to thank those who helped in the path leading to my graduation. First of all, my gratitude goes to Dr. Stefan Horender, who took good care of me, and whom I appreciated both professionally and personally. Also, my gratitude goes Dr. Mark Sawley, for his suggestions and his cheerful attitude. Thanks to Dr. Konstantina Vasilatou for her support and kindness. Moreover, I thank all the people I met at METAS, a bright environment where I had the most pleasant coffee breaks. To Dr. Michaela Eß, Daniel Kalbermatter, Dr. Karin Stettler, Dr. Maitane Iturrate, Dr. Tobias Bühlmann, Georgi Tancev, Dr. Marc-Olivier André: my best wishes, and, *Arrivederci!*
Moreover, I would like to thank Prof. Dr. Michele Iovieno and Prof. Dr. Alfio Grillo for arousing my curiosity towards mathematics and fluid dynamics. Thanks to my colleague Leonardo Gant for all the fun and mutual support. Finally, my gratitude goes to Prof. Ettore Filippo Lo Nigro, for teaching me so much about science and life.
As for my father, my mother and my grandmother: words are not enough to thank you for your love and for giving me the strength to face new challenges.

Ringraziamenti

Questa Tesi di Laurea ha ricevuto fondi dal programma EMPIR - progetto 18HLT02 AeroTox, cofinanziato dagli Stati Membri - e dal programma di ricerca ed innovazione dell'Unione Europea Horizon 2020.

Prima di iniziare, vorrei ringraziare coloro che mi hanno aiutato nel lungo cammino universitario. La mia gratitudine va innanzitutto al Dott. Stefan Horender, che mi ha seguito con cura e che ho apprezzato sia professionalmente che personalmente. Ringrazio il Dott. Mark Sawley per i Suoi consigli e il Suo fare sempre allegro. Grazie alla Dott.ssa Konstantina Vasilatou per il Suo supporto e la Sua gentilezza. Ringrazio tutte le persone che ho incontrato al METAS, un ambiente brillante dove ho trascorso le più piacevoli

pause caffé. Alla Dott.ssa Michaela Eß, a Daniel Kalbermatter, alla Dott.ssa Karin Stettler, alla Dott.ssa Maitane Iturrate, al Dott. Tobias Bühlmann, a Georgi Tancev, al Dott. Marc-Olivier André: i miei migliori auguri, e, *Arrivederci!*

Vorrei inoltre ringraziare il Prof. Dott. Michele Iovieno e il Prof. Dott. Alfio Grillo per avermi trasmesso il loro interesse verso la fluidodinamica e la matematica. Ringrazio il mio collega Leonardo Gant per tutto il divertimento e il reciproco supporto. Infine, la mia gratitudine va al Prof. Ettore Filippo Lo Nigro per avermi insegnato cosí tanto sia nella scienza che nella vita.

A mio padre, mia madre e mia nonna: le parole non sono abbastanza per ringraziarvi del vostro affetto e per avermi trasmesso la forza di affrontare nuove sfide.

Contents

1 Introduction

This master's project was born as a cooperation between the Swiss Federal Institute of Metrology (METAS) and EPFL. The work behind this thesis has been carried out entirely at METAS, exploiting its computational infrastructure and its laboratories. Fundamental was the advice and the expertise of METAS Partikle und Aerosol division, in particular of Dr. Stefan Horender and Dr. Konstantina Vasilatou, and of Dr. Mark Sawley, EPFL lecturer. Finally, this thesis contributes to AeroTox, a European Union's project. For further information about AeroTox, see `http://empir.npl.co.uk/aerotox/`.

1.1 Aerosols

The term aerosol is the abbreviation of *aerosolution*, from the Latin *aero*, air, and *solution*. It was created in 1920s in analogy to *hydrosol* (*21*). In everyday language, this term refers to the content of pressurized cans. In science, it is much more: according to (*9*), any *"collections of solid or liquid particles suspended in a gas"* constitute aerosols. In meteorology, aerosols are responsible for the formation of clouds, fog and mist. Nowadays, many research institutes focus on aerosols to understand the effects of air pollution on the human body and the environment. Aerosols have several industrial applications, as the production of pesticides, paints and cosmetics (*6*). Aerosols are classified according to the chemical nature of the solute particles or to their dimension. With respect to this, aerosol particles never have a single size, *e.g. 100 nm*. On the contrary, classification relies on *size distribution*, which can vary from few nm to about 100 μm (*22*). Above this limit, aerosols are not stable: particles have a high settling velocity and their drag law disappears quickly.

This master's project focuses on *simulated urban aerosols*. These are the suspensions commonly addressed as *air pollution*. Mostly, they comprehend carbon monoxide (CO), sulfur dioxide (SO_2), nitrogen oxides (NO_x), volatile organic compounds ($VOCs$), ozone (O_3), heavy metals, and respirable particulate matter (PM2.5 and PM10). To clarify, all the mentioned chemicals apart from the particulate matter are gases. Thus, they are grouped under the solvent phase of the aerosols, but their concentrations are increased by the anthropogenic activity and cause health issues (*19*). On the other

hand, *particulate matter* refers to a vast set of chemicals (*24*). Examples are *soot*, the product of engine combustion (thus including *black carbon* and other incomplete combustion products), *sodium chloride* and other *salts*, *dust* (mostly SiO_2 and Al_2O_3), *pollen*, etc. The composition of urban aerosols is strongly dependent on the anthropogenic activity and the natural environment. For instance, salt particulate is present in higher concentrations close to the sea, or during the cold season in Alpine environments (for safety reasons, salt is spread on the roads to decrease the cryogenic point of water).
Other factors contributing to the aerosol diversity are *chemical reactions*. Thanks to highly reactive compounds as ozone and NO_x and to solar radiations they are thousands and occur continuously.
It is now clear that only small fractions of urban aerosols can be reproduced in laboratories, where a defined set of substances and chemical reactions comes into play. However, according to the experiments to carry out, a significant collection of chemical species is utilized.

1.2 AeroTox

Over the years, health issues related to air pollution have become more and more common, raising the interest of both scientific community and public opinion (*19*). These diseases do not only affect the respiratory system, but also the cardiovascular (*12*) (*7*) and the digestive (*4*), and increase the stakes of developing cancer (*13*) and dementia. More in detail, according to the AeroTox scientific team, exposure to Particulate Matter (P.M.) 2.5 is responsible for almost 500000 premature deaths, causing the expenditure of 1600 bn $ a year (*35*) (to compare, about the 75% of the Italian GDP). The just mentioned data refers to Europe alone. The main goals of AeroTox are:

1. the development of standardized aerosols and reference aerosol calibration infrastructure;

2. creation of toxicological standards through the exposure of lung cells to fraction of simulated urban aerosols, both in vitro and in vivo. Correlation between the exposure and the health effects and between in vivo and in vitro acquired data;

3. the development of high-resolution imaging to highlight the effects of urban aerosols on lung cells;

4. the collection of reference material for the scientific community and the European citizens.

1.3 Overview of other relevant studies

A literature review regarding investigations of flows in mixing chambers has been performed. (*30*) analyzes slurry jets in a mixing chamber of a high-pressure abrasive slurry jet micro-machining (HASJM) system. Even if (*30*) does not consider any aerosols, an experimental and a CFD study of a flow in a mixing chamber is performed. CFD outcome is validated experimentally in the case of full flooding of the mixing chamber. Thus, CFD results are used to predict erosive efficacy at different working points than the full flooding. (*31*) performs unsteady Navier-Stokes CFD simulations of an air + SO_2 flow in a mixing chamber with two counter rotating fans at each end. Experimental validation is then performed, showing that both of the employed models (k-ω SST and SAS) deliver reasonable outcome, in particular the latter.
Finally, several papers (*14*), (*16*), (*26*) (*11*) and (*25*) apply CFD simulations to steam ejectors employed in refrigeration cycles. In particular, (*25*) exploits CFD (Fluent package, k-ω SST and realizable k-ε) to investigate the effects of the geometries of primary nozzles onto the ejector performances. Eight of those nozzles are tested, and the effect of the Mach number is addressed. However, the geometry of the mixing chamber is fixed *a priori*. Moreover, CFD outcomes are compared to experiments found in literature. The k-ω is better validated by the experiments and optimal conditions are reached using only one of the eight nozzles and a flow with a Mach number equal to 4. This study concludes that CFD is a suitable tool to investigate ejector performances and that the selected primary nozzles have great influence on them.
In conclusion, apart from (*32*), no studies relative to aerosol mixing chambers and the influence of their geometry were found. On the other hand, this literature review draws attention on different mixing chamber types and on successful CFD simulations. In some cases, those simulations are validated by experiments at specific working points of the systems, and then used to draw conclusions at different working points, which cannot be easily tested experimentally.

1.4 Goals

The general purpose of this master's project is to contribute to the design of the reference aerosol calibration infrastructure mentioned among the AeroTox goals. In other words, to develop a chamber where pure air and particles are mixed and the resulting aerosol has the most *homogeneous concentration* as possible. This master's project does not start from scratches. It continues the research carried out by the Partikle und Aerosol Labor, in particular by Dr. Stefan Horender, Mr. Kevin Auderset and Dr. Konstantina Vasilatou. Their current efforts are focused on reducing the dimension of the facility presented in (*32*). In terms of concentration, at the outlet their infrastructure presents a spatial homogeneity within 1.1%. The primary research question this master's thesis addresses is: *"how much can the mixing chamber dimensions be reduced without affecting the concentration homogeneity of the new born aerosol at its outlet?"* Indeed, this kind of chamber lies vertically. Also, the original METAS mixing chamber is more than 4 meter long. To use it, a dedicated laboratory is needed. Currently, the ideal target length has been set to less than a meter. This allows a comfortable usage and the possibility to easily transport the infrastructure. Another topic of discussion are the flow rates. The mixing chamber presented in (*32*) operates with a total airflow of 180 L/min. The infrastructure currently investigated at METAS is as big as $\frac{1}{3}$ of the original and needs only 60.5 L/min. Thus, the secondary research question is: *"how much can the mixing chamber airflow be reduced without affecting the concentration homogeneity of the aerosol?"* The reduction just pointed out is simply due to dimensions. Indeed, the longer chamber a flow of 120 L/min in the main pipe, whereas the shorter of 40 L/min. Their main pipes diameters measure 0.164 m and 0.051 m respectively. Therefore, the Reynolds number does not vary significantly ($Re_1 = 1035$ and $Re_2 = 1132$) and the two flows are equivalent. Instead, the current master's project aims at further reducing the flow rates, in order to diminish the Reynolds number too.

In addition, the designed mixing chamber should achieve satisfying concentration goals with different particle size distributions. Given the focus on urban simulated aerosols, the peaks in size distribution are presented in Figure 1. This aspect is mainly tested experimentally (see section 5), using salt particles (NaCl) and polystyrene latex (PSL).

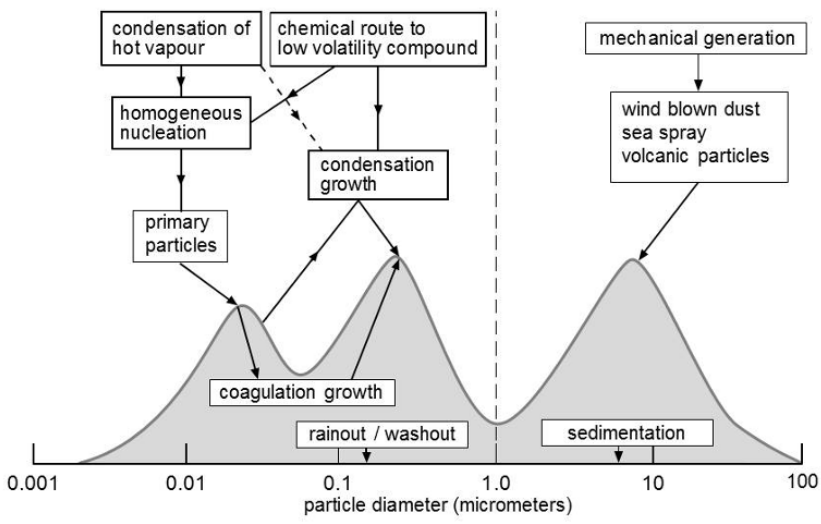

Figure 1: Size distribution of urban aerosol, showing peaks at 50 nm, 500 nm and 10 μm. Source:

1.5 Computational Fluid Dynamics (CFD)

Computational Fluid Dynamics consists in solving numerically the Navier Stokes (N.S.) equations, implementing specific algorithms on computers. The N.S. equation describe the motion of Newtonian fluids, but are extremely complicated to solve. They are a system of non-linear, coupled, Partial Differential Equations (PDEs). More in detail, their analytic solution exists and is known only in specific cases. There is no proof that such a solution exists for all flows. On the other hand, research and applied sciences are every day more interested in complicated flows, often unstationary or involving unusual 3D geometries. In many cases, CFD is the only tool to obtain whole fields of quantities related to the flow. For all these reasons, it finds many applications in nowadays world. Examples are the developing flow in a pipe, the combustion of air-gasoline mixtures in an engine, the aerodynamics of a vehicle, tomorrow's weather forecasts...

The expression *solving numerically* means approximating the PDEs describing the flow with solvable equations (*23*). As many options are available, the goal is to find simple equations which still model the phenomenon in a realistic manner. In every day language, the differences between exact and CFD

solutions are often addressed as *truncation errors*. However, this statement is incomplete. The main source of CFD inaccuracies are due to the solved equations being different, and thus the modelled phenomenon not entirely sticking to reality. This is the reason why phenomena as *artificial viscosity* take place. They have nothing to do with the flow, but only with the solved equations, which in this case allow a higher viscosity than the original ones. In conclusion, it is up to the ability of the user to model the flow properly. Fortunately, complete simulation software are now available and many of them feature useful Graphic User Interfaces (GUIs), where the most of the models/configurations are clearly pointed out.

The origins of CFD date back to the earliest approaches to the Navier-Stokes equations. Many common models were first conceived decades ago. An example is the k-ε turbulent model, which fundamentals were designed by Kolmogorov in the 1940s. Back then, computers were the bottleneck. Though, from the 1980s on, sufficient computational infrastructure became available. Consequently, huge efforts were performed to optimize algorithms, implement existing models and invent new ones.

Key elements of a CFD simulation are the *domain*, the *mesh*, the *boundary conditions* and the *selected equations*, be it a complete numerical simulation of the N.S. equations or the implementation of a simpler model (see subsection 3.1.2).

1.5.1 Advantages and Disadvantages

The construction of any infrastructures is a resource-demanding activity. In addition, design processes are rarely linear, but many times proceed by thinking and then discarding or confirming new ideas. The use of simulation software derives from the need of speeding design and testing related activities and of reducing costs. In addition to these general advantages, CFD simulations allow users to have *better understanding of the flow*, by *providing quantitative data* (values, functions, derivatives...) of all variables in every point of the domain. This is very complicated to achieve in experiments, and impossible to realize in the meantime. Moreover, *parametric geometries* are easily set up: this allows users to test different configurations/versions of the same product. Finally, *any boundary conditions* can be implemented.

On the other hand, CFD simulations can be misleading. Improper or simplified models, or wrong boundary conditions can easily lead to false results. Other sources of error are the number of computations per time step and interpolations. The resolution of the mesh plays a major role in the precision of the outcomes. To properly exploit CFD, users are supposed to understand the physical phenomena they are modelling and quantitatively imagine what the solution looks like. Hence, *validation* using observation/experiments is *necessary*. Moreover, today's professional software are often provided under strict licences, which hardly allow to export or postprocess files to/with other programs. In addition, when running complete CFD simulations as Large Eddy Simulations (LED) or Direct Numerical Simulations (DNS) (see subsection 3.1.2), computational costs rise and advanced infrastructures may be needed.

In conclusion, CFD simulations can bring benefits to design and test processes. They can be defined *virtual experiments*, but their findings have to be confirmed by real ones. For this reason, to achieve the goals of this master's project, both *CFD simulations* and *experiments* are performed.

2 Experimental Methodology

2.1 Setup of the Mixing Chamber

The mixing chamber this project refers to is the result of previous work performed at METAS and is presented in Figure 2. In particular, it is a smaller version of the chamber discussed in (*32*). It is a *modular structure*: it is the sum of an inlet pipe, a central segment and an exhaust pipe. By removing, adding or changing the central segments it can be elongated or shortened. This a major advantage to increase the *transportability*, one of the goals discussed in subsection 1.4. Starting from top, the mixing chamber features two sets of inlets. Those on the very top are welded on a flange clamped to the inlet pipe. Geometrically, they are aligned with the chamber's longitudinal axis. Instead, those on the side are inclined and thus are welded directly on the inlet pipe (CAD drawing in Figure 3). They are addressed as *slanted inlets*. All inlets have a diameter of 4 mm. Below the inlet pipe, the central segment connects to the exhaust, at the bottom. It is available in different lengths and determines the dimensions of the infrastructure. Instead, in-

let pipe and exhaust pipe have a fixed size. In every point, the diameter of the chamber is 5 cm. Finally, components are sealed to each other by *clamps*.

As shown in the longitudinal cross section in Figure 2, a probe is inserted from the from the outlet at the very bottom. It is the sampling tool used during experiments and connected to a particle counter. Thus, particle concentration is not measured at the very bottom of the pipe, but at the upper end of the probe, which is 22 cm long. Furthermore, the chamber is operated vertically: to prevent it from accidental tilting and falling, a holding structure is provided. It is connected to the mixing chamber through a clamp embracing the central segment of the pipe.

The structure of the chamber aims at increase mixing. On the very top, 7 are the inlets on the flange: 6 of them draw a circumference centered on the mixing chamber longitudinal axis. They all provide pure air. Instead, the seventh inlet is placed in the centre (in correspondence with the chamber's longitudinal axis), and injects a flow of both air and particles. The inlets on the side are inclined of 30deg with respect to the chamber's longitudinal axis. They are created on purpose to stimulate vortex structures for the mixing. These inlets inject pure air.

2.2 Reynolds Number

The Reynolds number is a *similitude parameter* which allows to extract the fundamentals of any flows. It is defined as follows:

$$Re = \frac{\rho U L}{\mu} = \frac{U L}{\nu} \tag{1}$$

where ρ is the fluid density, U its bulk velocity, L the characteristic length and μ the dynamic viscosity. The latter can also be expressed as $\mu = \nu \cdot \rho$, where ν is the kinematic viscosity. As the Reynolds number is the ratio of *inertia* to *viscous forces*, its physical meaning is the power relation between these two quantities. Except for the characteristic length and the bulk velocity, all variables involved in the Reynolds number represent fluid properties. In case of flow in a pipe, the characteristic length is the diameter of the pipe. Furthermore, when the Reynolds number is smaller than 2000, the flow is laminar. Its velocity field is ordered, there is high momentum diffusion and low convection. Thus, little or no mixing (only given by diffusion).

Instead, when the Reynolds number overcomes 2300, the flow becomes turbulent. This regime is chaotic, features high convection, dispersion, vortexes and swirls and thus provides high mixing.

The mixing chamber here analyzed presents different pipes (inlets and main pipe). Their diameters differ of an order of magnitude. When categorizing the flow regime, the choice between the Reynolds numbers is important. Indeed, with the operating flow rates, the two Reynolds numbers are one below and one above the transition value (≈ 2300). When considering the main pipe, with a diameter of 0.05 m and a total flow of 60 L/min, the resulting Reynolds number is 1700 (laminar). Instead, when considering the slanted inlets, with a diameter of 0.004 m and a total flow of 6.67 L/min, the resulting Reynolds number is 2400 (definitely turbulent). On the other hand, when leaving the inlets the nature of the flow cannot change so abruptly. The correct way to define the flow regime is to use the Reynolds number of the chamber region that influences the flow. Further insights about this topic are discussed is subsection 4.1.

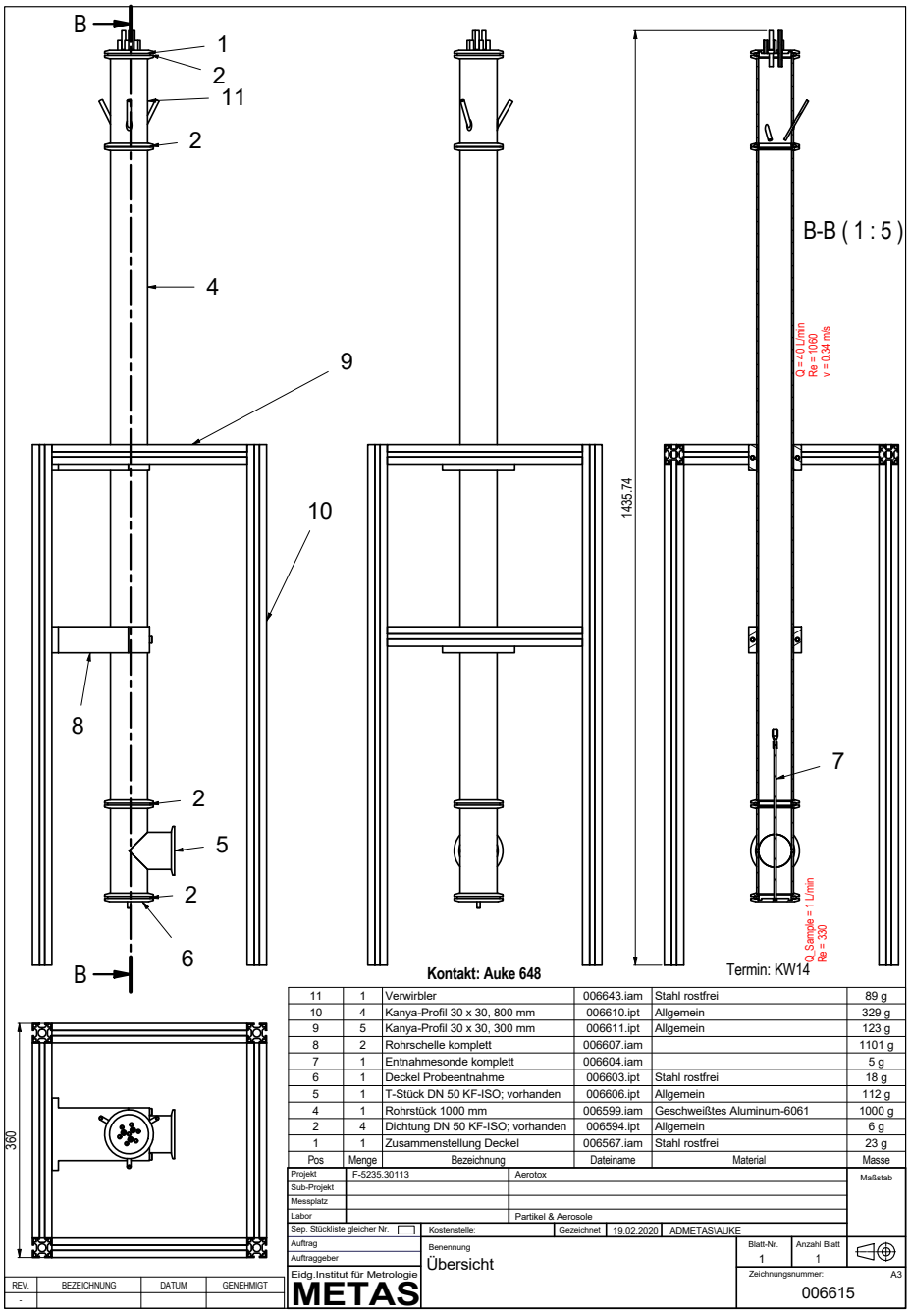

Pos	Menge	Bezeichnung	Dateiname	Material	Masse
11	1	Verwirbler	006643.iam	Stahl rostfrei	89 g
10	4	Kanya-Profil 30 x 30, 800 mm	006610.ipt	Allgemein	329 g
9	5	Kanya-Profil 30 x 30, 300 mm	006611.ipt	Allgemein	123 g
8	2	Rohrschelle komplett	006607.iam		1101 g
7	1	Entnahmesonde komplett	006604.iam		5 g
6	1	Deckel Probeentnahme	006603.ipt	Stahl rostfrei	18 g
5	1	T-Stück DN 50 KF-ISO; vorhanden	006606.ipt	Allgemein	112 g
4	1	Rohrstück 1000 mm	006599.iam	Geschweißtes Aluminum-6061	1000 g
2	4	Dichtung DN 50 KF-ISO; vorhanden	006594.ipt	Allgemein	6 g
1	1	Zusammenstellung Deckel	006567.iam	Stahl rostfrei	23 g

Projekt	F-5235.30113	Aerotox	Maßstab
Sub-Projekt			
Messplatz			
Labor		Partikel & Aerosole	
Sep. Stückliste gleicher Nr.	Kostenstelle:	Gezeichnet 19.02.2020	ADMETAS\AUKE
Auftrag			
Auftraggeber			

Benennung: Übersicht

Blatt-Nr. 1 | Anzahl Blatt 1

Eidg.Institut für Metrologie METAS

Zeichnungsnummer: 006615 A3

REV.	BEZEICHNUNG	DATUM	GENEHMIGT
-			

Figure 2: CAD drawing: frontal, side, top projection and longitudinal cross-section of the mixing chamber and its holding structure

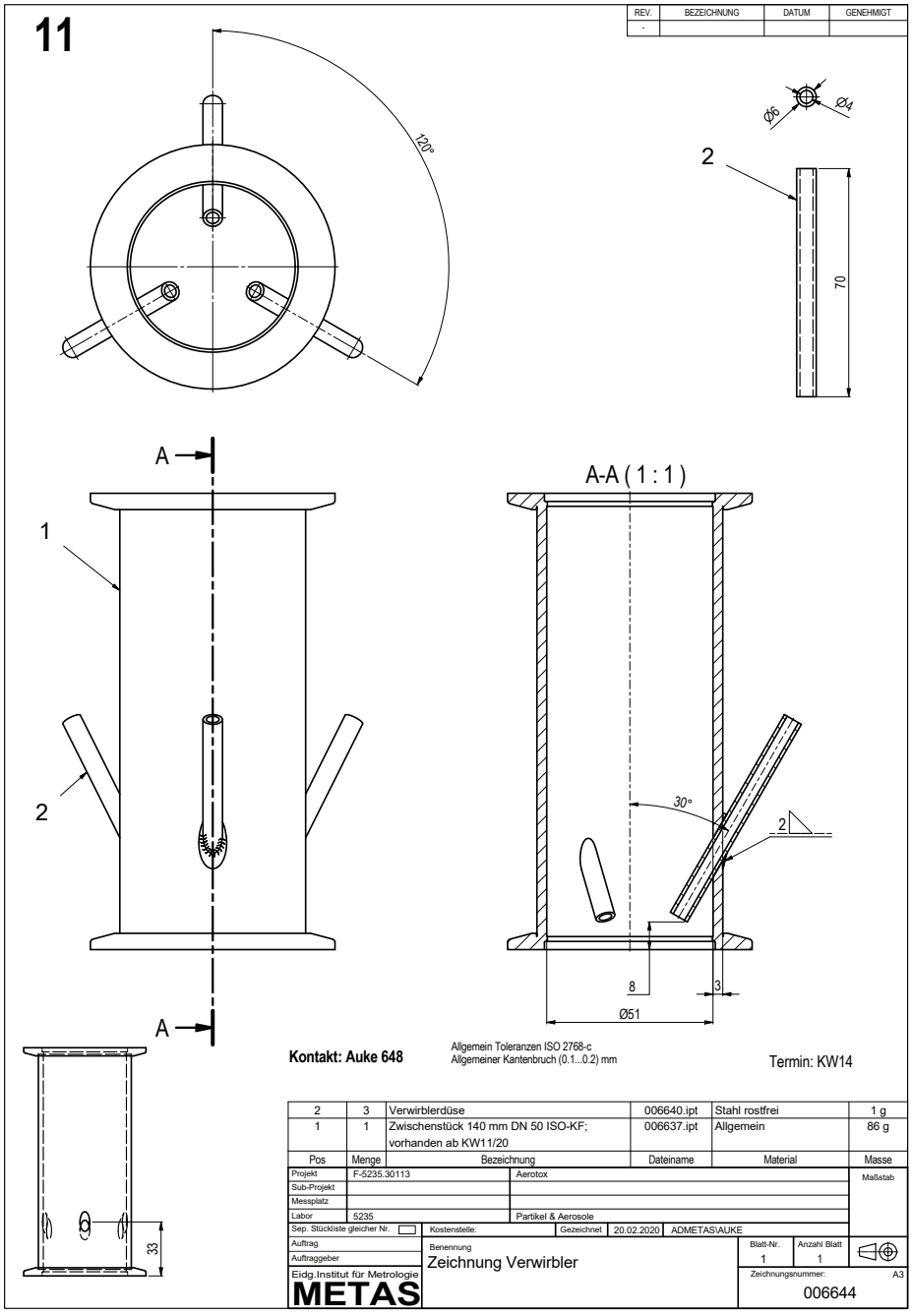

Figure 3: CAD drawing: top, frontal projection and longitudinal cross-section of the inlet pipe positioned on top of the mixing chamber

3 Numerical Methodology

In the following section, the chosen CFD software, the selected numerical models and the theory behind them are discussed. A brief introduction to turbulence and the mixing mechanisms is also provided.

3.1 Theoretical Premises

3.1.1 Turbulence and Navier Stokes equations

According to (*10*), the *"essential feature of turbulent flows is that the velocity field varies significantly and irregularly in both time and space."* More in detail, turbulent flows are chaotic flow regimes where energy is injected at large scales and is dissipated at small scales by viscosity. This transport mechanisms is addressed as *inertial cascade* and is caused by inertia. Qualitatively, turbulence is characterized by *streaks*, *strain regions* and *swirls*. Their interaction is complicated because they often merge and split. In addition to this, regions where the particles' vorticity is particularly high are named *eddies*. They involve different scales, from the dimension of the entire turbulent region down to that of a boundary layer. In particular, the higher the Reynolds number, the smaller the tiniest eddies will be. Quantitatively, turbulent flows are characterized by high Reynolds numbers. Thus, in all flow regions (apart from boundary layers), inertia prevails over viscous forces. Finally, the order of magnitude of the Reynolds number is equal to the ratio of the largest eddy scale to the smallest one.

The Navier-Stokes (N.S.) equations describe the motion of all Newtonian fluids. Solving them would unlock the complete knowledge any flows, including turbulent regimes. However, they are a set of coupled non-linear Partial Differential Equations (PDEs), and their analytic solution is unknown[1]. Moreover, there is no demonstration stating that an analytic solution always exists. In many cases, and especially when modelling turbulence, the N.S. equations are solved numerically.

[1]Precisely, analytic solutions exist for some specific cases, where some quantities or a dimension can be neglected. An example is *creeping flow*, where $\mathrm{Re} \ll 1$

3.1.2 Numerical Implementation of Turbulent Flows

There are two main ways to compute turbulent flows: solving the Navier-Stokes equations numerically, or making additional assumptions and build a so-called *turbulence model*. In the first case, Direct Numerical Simulations (DNS) come into play. They are computationally expensive, but calculate every scale of the turbulent flow. Typically, DNS are performed on powerful computing facilities. On the other hand, turbulent models neglect some scales: Large Eddy Simulations (LES) do not solve the smaller scales, nor do the k-ε models. Despite being less accurate, turbulent models are still valid and widely-used tools: they are computationally cheaper and most of them can be run on modest hardware.

3.1.3 Reynolds Averaged Navier-Stokes Equations

Despite being deterministic, turbulent systems are chaotic and thus non-reproducible. To overcome this limit, Reynolds developed a *statistical description* of turbulence by averaging in time all Navier-Stokes equations. He gave birth to the *Reynolds Averaged Navier-Stokes (RANS) equations*. Original N.S. quantities (as $u_i(x,t)$) are then described as follows:

$$u_i(\vec{x},t) = U_i(\vec{x},t) + u_i'(\vec{x},t) \tag{2}$$

where U is the time averaged value and u' the instantaneous fluctuations. According to the nature of the turbulent flow, averaged quantities are constant or time dependent. In case they are constant, the turbulent system is stationary and is commonly addressed as *statistically stationary*. Thus, average quantities lose their time dependence:

$$u_i(\vec{x},t) = U_i(\vec{x}) + u_i'(\vec{x},t) \tag{3}$$

Conversely, for unstationary turbulent flows equation 3 remains unchanged. Despite this, Reynolds averaging works as a *filter* and brings an advantage: the time variation of averaged values is much smoother than instantaneous fluctuations. In particular, the larger the time interval on which averages were performed, the smoother those averages will be. An example is provided in Figure 4.

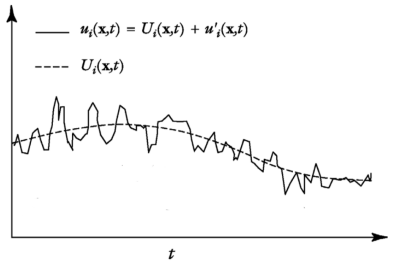

Figure 4: Smoothing effect of averaging process in an unsteady turbulent flow. The dot line is the average of the solid line. Source: (*33*)

RANS equations describing a statistically stationary flow are found below. They consider an incompressible fluid with constant properties (viscosity and density independent of temperature):

$$\frac{\partial U_i}{\partial x_i} = 0 \tag{4}$$

$$\rho U_j \frac{\partial U_i}{\partial x_j} = -\frac{\partial P}{\partial x_i} + \frac{\partial}{\partial x_j}(\tau_{ij} - \rho\overline{u'_j u'_i}) \tag{5}$$

with $\tau_{ij} = \mu(\frac{\partial U_i}{\partial x_j} + \frac{\partial U_j}{\partial x_i})$.
While equation 4 is scalar, equation 5 is vectorial. Thus, for such a system there are four linearly independent equations. Strictly speaking, RANS are not equivalent to the original N.S. equations: an additional tensor $(\rho\overline{u'_j u'_i})$ appears in the right hand-side of the momentum balance equation. It is addressed as *Reynolds stress tensor* and expresses the effects of instantaneous fluctuations on the average values. It comes out as a consequence of the averaging process, which gets rid of the time dimension. Its components bring in other 6 unknowns.

In conclusion, there are 10 unknowns: 3 velocity components, 6 Reynolds stresses and pressure. On the other hand, only four linearly independent equations are available: the system cannot be solved.

3.1.4 Closure models

To solve the RANS equations, *closure models* are necessary. Their intent is to make further hypothesis about the Reynolds stresses, express them independently of instantaneous velocities, and write additional equations. As a

consequence, solving the RANS equations means obtaining the average values of the velocity field, but not its fluctuations.

Over the years, many closure models have been formulated, each of them with advantages and shortcomings. It is in the interest of the user to check whether such assumptions are compatible with their specific flow.

3.2 Comparison of Different Software

Initially, the software considered to perform numeric simulations were COMSOL Multiphysics and ANSYS Fluent. The former uses a Finite Element Method (FEM) solver, whereas the latter a Finite Volume Method (FVM) solver. The main difference lies in the *conservative* nature of the FVM, clearly an advantage in CFD. Indeed, FVM defines a virtual volume (called control volume) for each mesh node and, exploiting the Green Gauss' theorem, transforms all volume integrals with divergence terms into fluxes. The sum of all fluxes of each cell is then null. On the contrary, in FEM the conservation of mass is not automatically verified. In addition, both software are known to be versatile, but in COMSOL it is possible to define and solve new PDEs. Instead, in ANSYS it is not designed for customized PDEs, but is in general more optimized and efficient with built in models. Finally, COMSOL has an intuitive Graphic User Interface (GUI) and is much more user-friendly than ANSYS.

For all the above reasons, COMSOL was selected over ANSYS. In addition, METAS has been purchasing COSMOL licence for more than five years. Carrying out this project with COMSOL is an opportunity for METAS to investigate whether another solver is necessary for CFD.

3.3 Numerical Models

3.3.1 k-ε Model

The k-ε is a closure model of particular interest, as it employs modest computational resources. Briefly, its additional equations are related to the transport of turbulent kinetic energy and its dissipation. Its hypothesis regards the turbulent viscosity and its main downside is that it does not perform well with adverse pressure gradients and low Reynolds number flows. This model

was first proposed (standard k-ε) in (*2*) and then improved in (*3*). Further details are given below.

To understand the main assumption of this model, a brief flashback is necessary. In 1877 Boussinesq linked the total stresses ($\tau_{tot} = \tau_{ij} - \tau_{turb} = \tau_{ij} - \rho\overline{u'_j u'_i}$) to the gradient of the average velocity field U (Boussinesq assumption):

$$\tau_{tot} = (\mu + \mu_T)\frac{dU}{dy} \tag{6}$$

Equation 6 is clearly an analogy to *Newton's shearing stress* equation:

$$\tau = \mu\frac{du}{dy} \tag{7}$$

In equation 7, the coefficient μ is the *dynamic viscosity*. It exclusively depends on the fluid and its state. Instead, in equation 6 the dynamic viscosity is corrected with a so-called *eddy* or *turbulent viscosity*, which depends on the velocity of the fluid. This is the only way to work out the relation, as the turbulent stresses are quadratically proportional to the velocity. (*10*) and (*27*) show that equation 9 can be simplified defining the *mixing length* scale l_m. They come up to the following expressions:

$$\nu_T = \mu_T/\rho = l_m^2\frac{dU}{dy} \tag{8}$$

and thus:

$$\tau_{turb} = l_m^2(\frac{dU}{dy})^2 \tag{9}$$

which definitely show that μ_T depends on the average velocity field.

On the other hand, the k-ε model is based on the turbulent viscosity assumption by Prandtl and Kolmogorov. According to dimensional analysis, they defined it as:

$$\nu_T := c\frac{k^{\frac{1}{2}}}{l_m} \tag{10}$$

However, since the turbulent kinetic energy and the turbulent dissipation are defined as:

$$k := \frac{1}{2}u'_i u'_j \tag{11}$$

$$\varepsilon := C_\varepsilon \frac{k^{\frac{3}{2}}}{l_m} \tag{12}$$

in the k-ε model the turbulent viscosity is defined as:

$$\nu_T = C_\mu \frac{k^2}{\varepsilon} \tag{13}$$

Finally, the main assumption of this model lies in the *isotropy of the turbulent viscosity.*

The previous assumption alone is not sufficient to close the problem. Hence, the k-ε considers two additional transport equations:

$$\frac{\partial k}{\partial t} + U \cdot \nabla k = \nabla \cdot ((\nu + \frac{\nu_T}{\sigma_k})\nabla k) + P_k - \varepsilon \tag{14}$$

$$\frac{\partial \varepsilon}{\partial t} + U \cdot \nabla \varepsilon = \nabla \cdot ((\nu + \frac{\nu_T}{\sigma_\varepsilon})\nabla \varepsilon) + C_{\varepsilon 1}\frac{\varepsilon}{k}P + C_{\varepsilon 2}\frac{\varepsilon^2}{k} \tag{15}$$

where P_k represents the production of turbulent kinetic energy. The first equation is *exact*, whereas the second is an analogy for the dissipation ε. In both of the equations, the first term on the left hand-side can be seen as a Lagrangian derivative of k or ε expressed in spatial coordinates ($\frac{Dk}{Dt}$ and $\frac{D\epsilon}{Dt}$). Finally, coefficients $C_{\varepsilon 1}$ and $C_{\varepsilon 2}$ are determined experimentally.

Wall Functions

Close to the wall, the basic assumption of the k-ε model is not valid. In the boundary layer, dissipation reaches its peak, and turbulent viscosity its minimum. To overcome this problem, the last mesh cell does not touch the wall, but leaves a small gap, called *lift-off* (δ_w^+). The lift-off is expressed in viscous units, which are pure numbers:

$$\delta_w^+ = \frac{\delta_w u_t}{\nu} \tag{16}$$

where $u_t = \sqrt{|\tau_w/\rho|}$ is the *friction velocity* and τ_w the stress tensor evaluated at the wall. Through the lift-off, the flow is computed using analytic functions called *wall functions.* As an example, the velocity is calculated following Von Karman's logarithmic law:

$$U^+ = \frac{U}{u_t} = \frac{1}{k_v} log(\delta_w^+) + B \tag{17}$$

where k_v is the Von Karman's constant. The universality of this law was validated experimentally: for many flows, $k_v = 0.4$ and $B = 5.2$. The boundary conditions applied to the velocity are the no penetration condition and a shear stress condition. The latter ensures matching between the stress tensor obtained with the velocity and the stress tensor calculated with pressure.
As shown, the wall functions do not consider the subviscous layer, but only the logarithmic law. To further improve the wall flow region, the k-ε model can be modified, giving birth to the *low-Re k-ε model*. This model exploits a very thin mesh close to wall, but is computationally expensive.

3.3.2 Particle Tracing for Fluid Flow

Lagrangian vs Eulerian

When modelling the motion of a particle in fluid flows, two descriptions can be employed: the *Lagrangian* (also known as *material*) and the *Eulerian* (also known as *spatial*). The former implies the observer to be integral with the particle, whereas the latter focuses on a so-called control volume. When this is the case, conservation laws or balance equations relative to all quantities are written. The Eulerian perspective is clearly simpler, especially in experiments: taking any kind of measurements in a fixed position is much simpler than following a moving object. When it comes to practice though, equations are treated with numerical solvers and stability issues must be considered. In case of a Finite Element Method solver (as COMSOL Multiphysics), the Lagrangian description implies no restrictions on the Peclet [2] number: stability is always ensured. For this reason, only the material description is treated in this chapter.

Mixing mechanisms

In case of turbulence, two are the mechanisms contributing to the mixing of particles (dispersed phase) in a flow (continuum phase): *dispersion* and *diffusion*. The former is due to the chaotic nature of turbulence and its complicated flow structure, made of vortexes, eddies and swirls. Conversely, the latter interests any situations featuring spatial concentration gradients.

[2] The Peclet number is a similarity parameter obtained as the ratio of the rate of advection of a quantity by the flow over the rate of diffusion in the same flow.

Dispersion

To better understand dispersion, one should think of a simple definition of turbulence: a chaotic regime, thus extremely non linear, where the flow dissipates energy through viscous effects (*27*). Qualitatively, a turbulent flow is characterized by fluctuations of vorticity. Also, it is made of *streaks*, *strain regions* and *swirls*. Their interaction is complicated because they often merge and split. Furthermore, the mixing of mass, thermal energy and momentum reaches its maximum in the *eddies*, regions where the particles' vorticity is particularly high. Mathematically speaking, the mixing of particles can be understood from the definition of chaotic system. Such a system is deterministic, but the slightest change in the initial conditions causes the deriving solutions to be unpredictably different. In the current case, this is great news: despite particle injection is performed in a little portion of the inlet of the mixing chamber, their resulting position will be different. This mechanisms is addressed as *turbulent dispersion*.

Diffusion

From the Latin *diffundere*, to spread out, diffusion is a physical phenomenon which takes place on different scales. It can be molecular or atomic, in which case it is addressed as *brownian motion*. As mentioned above, being it proportional to the opposite of the gradient, diffusion smooths out any concentration differences. Generally, diffusion is modelled by Fick's Law:

$$J = -D\frac{\partial c}{\partial x} \tag{18}$$

where J indicates the mass flux along the reference coordinate (x), c indicates the dispersed phase concentration and D is the *diffusivity*, a coefficient depending on the nature of the dispersed phase. It is important to highlight that in *ensembles*, diffusion does not *move* particles, but it simply spreads them. Their averaged displacement will be null. Finally, when modelling Brownian motion, *random walk* often comes into play. In particular, this is implemented when the goal is to simulate the motion of particles following the Lagrangian description in a turbulent flow.

Coupling

The term *coupling* has both a mathematical and a physical meaning. It refers to the influence of one phenomenon onto another. This topic is of particular interest in scientific computation, because the impacts of two or more phenomena onto each other must be carefully quantified. To keep it simple, let's analyze the current case. It is clear that the dispersed phase is transported by the continuum one, but does the presence of the former *significantly* influence the latter? The affirmative case results in a *two-way coupling*, whereas the negative in a *one-way coupling*. To respond to that question, one must remember that the given aerosol is highly diluted. As shown below, the volume fraction ϕ_{vD} of the dispersed phase is estimated to be smaller than 1% of ϕ_{vC}, the volume fraction of the continuum phase.

$$V_{chamber} \approx \pi \cdot 2.5^2 \cdot 75 = 1463cc \approx 1.5 \cdot 10^3 cm^3 \tag{19}$$

ϕ_v is estimated by accounting for approximately 10^4 particles per cubic centimeter ($d = 1\ \mu m$):

$$N_{particles} \approx 1.5 \cdot 10^3 \cdot 10^4 = 1.5 \cdot 10^7 \tag{20}$$

and then

$$N_{particles} \cdot V_{particles} \approx 1.5 \cdot 10^7 \cdot 4 \cdot (0.5 \cdot 10^{-6})^3 \approx 7.5 \cdot 10^{-12} m^3 \tag{21}$$

and

$$\frac{\phi_{vD}}{\phi_{vC}} = \frac{N_{particles} \cdot V_{particles}}{V_{chamber} - N_{particles} \cdot V_{particles}} \approx 10^{-6} < 0.01 \tag{22}$$

Despite this, before rushing to the *one-way coupling* option, (*20*) suggests to evaluate the mass fraction ϕ_m too. Logically, the mass fraction is determined multiplying the volume fraction by the ratio of the respective densities:

$$\phi_{mD} = \phi_{vD} \cdot \frac{\rho_{dispersed}}{\rho_{continuum}} \tag{23}$$

In conclusion, even if the density ratio is:

$$\frac{\rho_{dispersed}}{\rho_{continuum}} = \frac{2200\ \mathrm{kg/m^3}}{1.2\ \mathrm{kg/m^3}} \approx 1800 \tag{24}$$

both ϕ_{mD} and ϕ_{vD} are negligible. Thus, as shown in (*20*), the one-way coupling option can be safely picked.

In general, the coupling options among which one has to choose are not only the one-way and two-way coupling. By increasing the mass and the volume fraction of the dispersed phase, mutual particle interactions have to be taken into account. This case goes under the name of *four-way coupling*. Below, a summarizing picture (Figure 5) from the COMSOL Multiphysics manual (*34*) is shown. Here, the above mentioned coupling options are listed. At the bottom of the image, the ultimate case is displayed: mass and volume fraction are so high that the mathematical description of the model is insufficient. The computation is then unsuccessful.

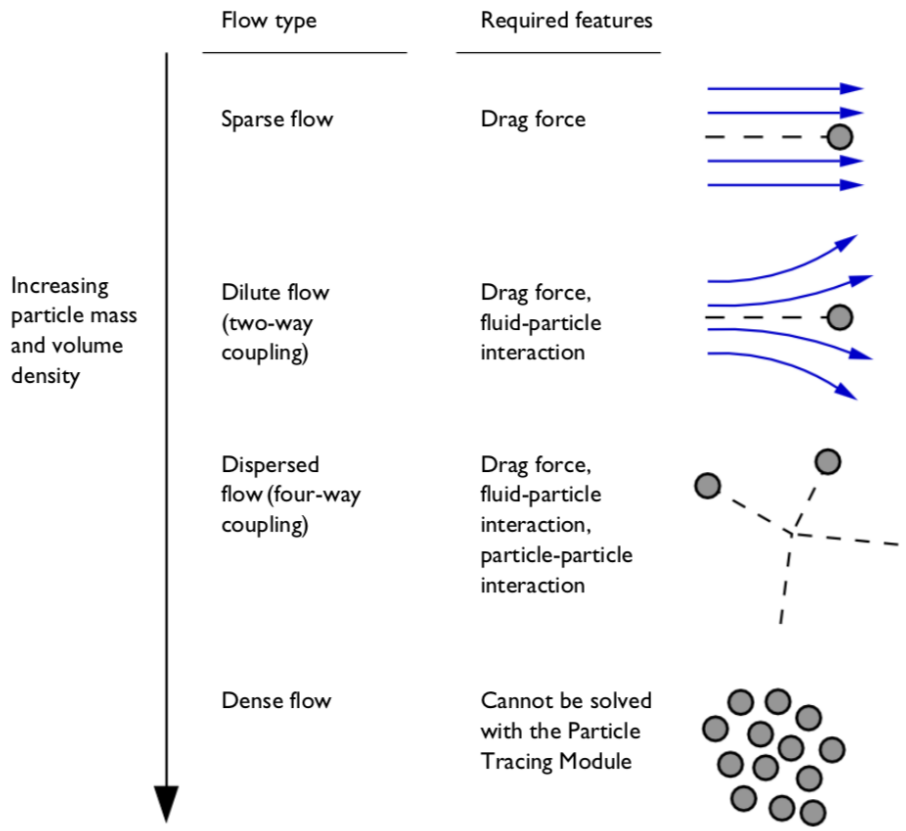

Figure 5: One-way (Sparse flow), two-way (Diluted flow) and four-way (Dispersed flow) coupling modalities; Dense flow (solver unsuccessful). Source: (*34*)

Mathematical Formulation

While implementing a Lagrangian description of the particle motion, the computer solves an Ordinary Differential Equations (ODEs) per time step. They all correspond to Newton's Second Law of dyamics:

$$\frac{d}{dt}(m_p\vec{v}) = \vec{F_{ext}} \tag{25}$$

where m_p represents the particle mass, $\vec{v}$ is the particle velocity vector ($\vec{v} = \frac{d\vec{q}}{dt}$, $\vec{q}$ being the particle position vector) and $\vec{F_{ext}}$ is the sum of all external forces applied on the particle. In the present case, particle mass does not vary in time. Thus, the previous equation becomes:

$$m_p\frac{d}{dt}\vec{v} = \vec{F_{ext}} \tag{26}$$

It is now fundamental to list all external forces applied on the particles:

- Particle-fluid flow interaction force;
- Gravity force;
- Buoyancy force.

The first element is clearly fundamental because it depends on the difference between particle and fluid velocities (see previous subsection). The kind of dependence will be determined by the Reynolds number. Conversely, gravity and buoyancy forces significance has to be evaluated.

Particle-fluid flow interaction force

The Reynolds number of the flow around the particle is:

$$Re_p = \frac{d_p(U-V)}{\nu} \tag{27}$$

In order to understand the dominant flow regime, it is necessary to calculate the maximum value of the Reynolds number. Thus, let's select

- $U = 10$m/s, as the maximum speed found when computing the flow with the K-ϵ turbulent model is approximately 25m/s;

- $V = 0\text{m/s}$, to imagine the worst possible scenario: the particle is injected with null speed in the fastest portion of the flow.

Then, the *highest possible* Reynolds number is:

$$Re_p = \frac{d_p(U-V)}{\nu} = \frac{10^{-6} \cdot 10}{1,5 \cdot 10^{-5}} = 0.67$$

It is probably overestimated by an order of magnitude, thus viscous forces prevail upon inertia. Therefore, the selected interaction force in the solver is *Stokes drag*, according to which:

$$F_{St} = 6\pi\mu r_p(\vec{u} - \vec{v}) \tag{28}$$

where $\vec{v}$ is the particle velocity, and $\vec{u}$ the fluid velocity.

Stokes law is obtained from the Navier-Stokes equations (*27*). To do so, it is necessary to *non-dimensionalize* them and get rid of the negligible terms exploiting the low Reynolds number assumption. The creeping flow equations are then obtained. They are know for their particular properties, one of them being *time-reversibility*. Now, Stokes law is obtained integrating the pressure on the surface of a sphere.

Stokes Drag vs Aerodynamic Forces

Analyzing Stokes drag law, it is interesting to notice that the dependence on the velocity is not squared, but linear. When dealing with higher Reynolds numbers, aerodynamic forces are quadratically proportional to the velocities, indeed:

$$D = \frac{1}{2}\rho V^2 C_D S \tag{29}$$

Aerodynamic forces are directly proportional to the *dynamic pressure* times the interested surface. The proportionality coefficient C_L or C_D depends on the specific case (Reynolds number, shape of the body, ...) and is usually determined experimentally (see Figure 6).

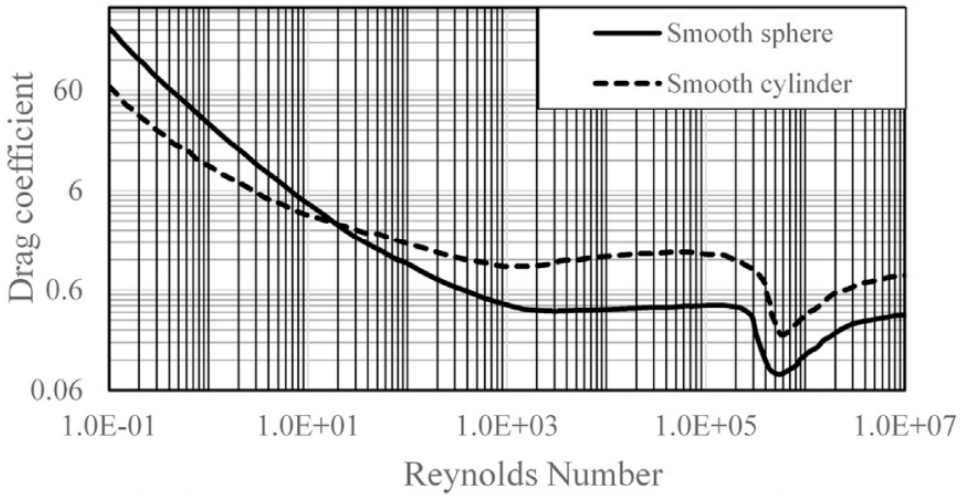

Figure 6: Experimentally determined drag coefficient C_D against Re of ideal sphere or circular cylinder. Source: (*28*)

More in detail, when $Re \ll 1$, $C_D = \frac{24}{Re_r}$.[3] By substituting for this coefficient in the previous relations, one obtains Stokes drag law.

$$C_D = \frac{24}{Re_r} \tag{30}$$

$$Re = \frac{\rho V 2r}{\mu} \tag{31}$$

$$S = \pi r^2 \tag{32}$$

$$D = \frac{1}{2}\rho V^2 C_D S = \frac{1}{2}\rho V^2 \frac{24\mu}{\rho V 2r}\pi r^2 = 6\pi\mu r V = F_{St} \tag{33}$$

In the lines above, V indicates the difference between the body's velocity and the velocity of the fluid it is immersed in. Furthermore, a body's interested surface is the projection of its total surface on the frontal plane (as for the sphere, $\frac{1}{4}$ of S_{tot}).

[3] Re_r meaning *Reynolds number relative to the immersed body*

Gravity and Buoyancy force

Since the infrastructure is designed to lie vertically, the longitudinal direction of the cylinder (and thus the bulk velocity of the flow) will be aligned with gravity. Therefore, gravity and buoyancy forces must be taken into account. A quick manner to evaluate their impact on particle motion is to calculate the *settling velocity*, [4] which is their ultimate and maximal free-falling velocity in a fluid. When this condition is matched, drag, gravity and buoyancy balance out, and there is no net force acting on the particle:

$$\vec{F_{St}} + \vec{F_g} + \vec{F_{buoy}} = \vec{0} \tag{34}$$

The modulus of gravity and buoyancy forces combined is:

$$|\vec{F_g} + \vec{F_{buoy}}| = m_p g \frac{\rho_p - \rho_f}{\rho_p} \tag{35}$$

Considering only z direction, one obtains:

$$m_p g \frac{\rho_p - \rho_f}{\rho_p} - 6\pi\mu r_p V = 0 \tag{36}$$

and, since $m_p = \rho_p \cdot \mathrm{Vol}_p$ ($m_p \approx 1.15 \cdot 10^{-15}\mathrm{kg}$)

$$V = \frac{g(\rho_p - \rho_f)\frac{4}{3}r^2}{36\mu^2} = 6.67 \cdot 10^{-5}\mathrm{m/s} \tag{37}$$

In conclusion, the settling velocity is smaller than a tenth of millimeter per second. Moreover, it depends neither on time nor on position. On the other hand, the absolute minimum of the flow bulk velocity has an order of magnitude of 10^{-1}m/s, almost a four orders of magnitude higher. For these reasons, gravity and buoyancy force can be neglected.

Despite the gravity force is negligible, it is interesting to notice how it prevails over buoyancy. Calculating the settling velocity without considering buoyancy, one obtains:

$$V^* = \frac{m_p g}{6\pi\mu r_p} \tag{38}$$

[4] Also know as *terminal velocity*.

Thus, the relative error is:

$$\text{err}\% = 100 \cdot \frac{V^* - V}{V} = 100 \cdot (\frac{\rho_p}{\rho_p - \rho_f} - 1) = 0.056\% \tag{39}$$

In conclusion, gravity and buoyancy are both neglected because of their minimal effect on particle motion. Despite this, buoyancy could be neglected with respect to gravity.

The last result can be guessed. Indeed, buoyancy is directly proportional to the ratio of fluid to particle density, which is in this case very small ($\approx 5.57 \cdot 10^{-4}$). Generally, since the air has such a low density compared to any solid bodies, buoyancy is not considered in aerodynamics.

Initial Conditions

In the end, the equation to solve is:

$$m_p \frac{d}{dt}\vec{v} = 6\pi\mu r_p(\vec{u} - \vec{v}) \tag{40}$$

and the unknown is the particle velocity $\vec{v}$. Since it is a vectorial equation, all three directions have to be solved. From now on, only the first direction (addressed as "$_1$") is considered and the equation becomes thus scalar. This is possible because the three directions are not coupled. Writing it in canonic form:

$$\dot{y}(t) + \frac{b}{m_p} y(t) = \frac{b}{m_p} u \tag{41}$$

where $y = v_1$, $\dot{y} = \dot{v_1}$, $b = 6\pi\mu r_p$ and $u = u_1$. It is now clear that it is a linear, first order non-homogeneous Ordinary Differential Equation (ODE). Thus, a (existing) unique solution is expected. By solving the associated homogeneous equation, one gets:

$$\frac{d}{dt}(e^{\frac{b}{m_p}ut} y(t)) = 0 \implies y(t) = Ae^{-\frac{b}{m_p}ut} \tag{42}$$

Therefore, solving the complete equation one gets:

$$\frac{d}{dt}(e^{r(t)} y(t)) = e^{r(t)} \frac{b}{m_p} u \tag{43}$$

$$y(t) = e^{-r(t)} \int \frac{b}{m_p} u e^{r(t)} dt \tag{44}$$

$$y(t) = e^{-r(t)} \frac{b}{m_p} u \int e^{r(t)} dt = \frac{b}{m_p} u e^{-r(t)} [\frac{1}{\dot{r}(t)} e^{r(t)} + C_1] \tag{45}$$

where

$$r(t) = \int \frac{b}{m_p} dt = \frac{b}{m_p} t$$

and

$$\dot{r}(t) = \frac{b}{m_p}$$

In conclusion, the *general integral* of the original equation is:

$$y(t) = u + C_1 \frac{b}{m_p} u e^{-\frac{b}{m_p} t} \tag{46}$$

Using the original notation:

$$v_1(t) = 1 + C_1 \frac{6\pi\mu r_p}{m_p} u_1 e^{-\frac{6\pi\mu r_p}{m_p} t} \tag{47}$$

To obtain the *particular solution*, one condition (C_1) is needed: the initial velocity. In reality, the solver treats the previous equation as a second order differential equation, and determines the position of the particle. In that case, two initial conditions are required: the *initial velocity* and the *initial position*.

Time and Length Scales

As outlined in the subsection just above, solving for the particle velocity requires the knowledge of the fluid velocity field. At first, this seems a problem because the fluid flow was computed using a k-ε (and thus RANS based) turbulent model. In conclusion, the performed calculation revealed only the average values of the velocity field, without providing further information about its instantaneous fluctuations. To overcome this issue, velocity oscillations are simulated by a *discrete random walk*, a statistical process where at each time step, a given increment is added the previous value. Such an increment is kept constant for the whole *time a particle interacts with an eddy*. Therefore, in every point of the domain:

$$\vec{u'} = \vec{u} + \vec{\Delta u}, \tag{48}$$

where $\vec{u'}$ is the local fluid velocity, $\vec{u}$ is the local averaged velocity (from RANS equations) and $\vec{\Delta u}$ represents the instantaneous fluctuation. Moreover,

$$\vec{\Delta u} = \zeta\sqrt{\frac{2k}{3}} \tag{49}$$

where ζ is a random variable and k is the turbulent kinetic energy obtained from the solution of the k-ε model. Then, the only remaining question is how to evaluate the time a particle interacts with an eddy. According to (*5*), this interval is the lesser between the average eddy lifetime (τ_e) and the *average time a particle takes to cross it* (τ_c). Moreover, by assuming that the *average eddy size* corresponds to the dissipation length scale $l_e = \frac{C_L^{\frac{1}{2}} k^{\frac{3}{2}}}{\varepsilon}$, one finds:

$$\tau_e = \frac{k}{\varepsilon} \tag{50}$$

where C_L is a dimensionless coefficient usually in between 0.2 and 0.96 (see (*17*)). Furthermore,

$$\tau_c = -\tau_p \log(1 - \frac{l_e}{\tau_p|\vec{u} - \vec{v}|}), \tag{51}$$

where τ_p is the particle *relaxation time*. In COMSOL Multiphysics, both τ_e and τ_c are calculated automatically and the time step is chosen accordingly (a couple of orders of magnitude smaller than the lesser of them). Moreover, the solver time step must be smaller than the relaxation time (τ_p) too. To determine this quantity, one has to write the discrete version of Newton's Second Law:

$$F_{ext} = \frac{1}{\tau_p} m_p(|\vec{u} - \vec{v}|);$$

As explained in the previous subsection, Stokes drag is the only significant external force applied to the particles. Thus,

$$F_{Stokes} = 3\pi\mu d_p(|\vec{u} - \vec{v}|).$$

$$F_{ext} = F_{Stokes} \implies \frac{1}{\tau_p} m_p(|\vec{u} - \vec{v}|) = 3\pi\mu d_p(|\vec{u} - \vec{v}|)$$

$$\tau_p = \frac{m_p}{3\mu d\pi}$$

Now, one can substitute for $m_p = \rho_p V_p$ and $V_p = \frac{4}{3}\pi r_p^3$, obtaining:

$$\tau_p = \frac{d_p^2 \rho_p}{18\mu} \tag{52}$$

Here, the relaxation time $\tau_p \approx 7 \cdot 10^{-6}$ s. Even in this case, the solver automatically picks a time step two orders of magnitude smaller than the just derived parameter.

3.3.3 Transport of Diluted Species

The following subsection explores the possibility of treating the aerosol as two chemical species: a solvent and a solute; the latter being present in much smaller concentrations.

Mixing Mechanisms

The mixing mechanisms are related to concentration gradients and Brownian motion, thus diffusion. The key equation implemented during simulations is:

$$\frac{\partial c_i}{\partial t} + \nabla \cdot \vec{J_i} + \vec{u} \cdot \nabla c_i = R_i \tag{53}$$

where c_i represents the concentration of the solute, $\vec{J_i}$ the diffusion term, $\vec{u}$ the velocity vector and R_i the sink or source. The third term of the left hand-side represents *convection*, which has not named among the mixing mechanisms a few lines above. Strictly speaking, the convective term originates from the motion of the fluid; however, the concentration gradient appears in the formulation of convection ($\vec{u} \cdot \nabla c_i$). The manifest connection between the two phenomena can be shown mathematically by writing the Lagrangian derivative in spatial coordinates:

$$\frac{Dc_i}{Dt} = \frac{\partial c_i}{\partial t} + \vec{u} \cdot \nabla c_i \tag{54}$$

In the right hand-side, the first term refers to local variation, whereas the second to originates from motion and has global impact. Therefore, equation 53 can be simply expressed as:

$$\frac{Dc_i}{Dt} + \nabla \cdot \vec{J_i} = R_i \tag{55}$$

Furthermore, the mixing chamber can be seen as a pipe featuring a source at the inlet and a sink at the outlet. Both source and sink are *time independent*. In addition, their effects compensate and the quantity of solute in the chamber is constant in time. Then, $\frac{\partial c_i}{\partial t}$ is the only time-dependent term and is thus constant. In the stationary case here analyzed, it is set to zero.

Summarizing, since the transient case is of no interest in this analysis, all concentration time dependencies are set to zero. The remaining mixing phenomena are represented by convection and diffusion divergence. Sink and source terms are time independent too, because the quantity of solute in the mixing chamber is constant. In addition, the right hand-side of equation 53, equals zero, because the mixing chamber source (at the inlet) and its sink (at the outlet) balance out. The only way to have a stationary case (thus with time *independent* local concentrations) while keeping non-balanced sinks and sources, is by considering an infinite domain. Otherwise, the solute will accumulate and local concentrations will rise (or viceversa). On the other hand, sink and source being time independent is no *sufficient* statement for *stationarity*. It is only a *necessary* condition.

Equation 53 can be written in a conservative or non-conservative form. In case the fluid is incompressible ($\nabla \cdot \vec{u} = 0$), they are equivalent. However, algorithms operate differently. In this project, the default value was picked ().

As mentioned in section 3.3.2, diffusion can be modelled by Fick's Law (see Equation 18). The diffusion coefficient, or *diffusivity*, can be determined thanks to Einstein's relation:

$$D = \frac{k_B T}{6\pi\mu r_p} \tag{56}$$

where k_B represents Boltzmann's constant and T the absolute temperature of the system. Then, particles having 1μm diameters have a diffusion $\approx 10^{-10} m^2/s$. When the flow velocity determines a turbulent regime, dispersion prevails over diffusion and is responsible for turbulent mixing. However, this mechanism is not directly taken into account by equation 53. Indeed, when implementing a turbulent model (be it RANS or LES), small eddies are not resolved. Therefore, the term $\frac{\nu_T}{Sc_T}$ is added to the diffusivity:

$$D_{tot} = D + \frac{\nu_T}{Sc_T} \tag{57}$$

and a proper mixing is obtained. More in detail, v_T represents the *eddy viscosity* (turbulent momentum diffusivity) and Sc_T the *turbulent Schmidt number*. The latter is defined as:

$$Sc_T = \frac{v_T}{K_T} \tag{58}$$

where K_T represents the turbulent mass diffusivity. Values of Sc_T are always determined experimentally, typically ranging between 0.2 and 1.3. Unfortunately, this interval is wide and the choice affects diffusion remarkably. Wisely, (*18*) suggests to look at the dominant flow and provides examples of dispersion around buildings, in boundary layers and in axisymmetric flows. The latter resembles the mixing chamber here treated, thus the Schmidt turbulent number is chosen to be 0.7.

Numerical Diffusion

In CFD, the fictitious and augmented diffusion (even of one order of magnitude) is addressed as *numerical diffusion*. As mentioned above, the continuum perspective does not directly account for dispersion, but applies a correction to increase Brownian diffusion. Thus, the impact of this phenomenon is high, and checking whether the obtained diffusion is artificial is *fundamental*.

According to (*1*), numerical diffusion consists in a simple truncation error. A brief literature review confirms that about 50 years ago, this idea was spread. Back then, many papers provided simple estimates of numerical diffusion (seen as a truncation error). On the contrary, the article just cited provides formulae to determine such an error and select time steps to contain its effects.

Nowadays, numerical diffusion has a different definition. It is generated by a subset of truncation errors following discretization. More in detail, it comes into play when the solver is unable to determine the correct direction of the flow. Then, convection comes in and wrong mass transport follows. (*29*) classifies numerical diffusion related errors into two categories: *cross-stream* and *streamwise*. The former takes place when high gradients are perpendicular to the flow direction and oblique with respect to the cell boundary. The latter when steep gradients are parallel to the flow direction.

In order to understand whether the studied problem gives birth to severe numerical diffusion, some test simulations are carried out. The main idea is to create a domain similar to that of the mixing chamber, while stressing the characteristics which could lead to numerical diffusion. Therefore, the domain presented in Figure 7 has been made up. It consists of a straight pipe with two inlets: one on top and one downstream on the side. Moreover, the flow direction follows the longitudinal axis of the pipe as most of the air comes from the top inlet (more than 95% in volume). As for the chemical aspect, only one solute is considered and it enters the facility from the inlet on the side. It has a concentration of $10[mol/m^3]$ and a diffusivity of $D = 10^{-10}m^2/s$. This way, there is a high concentration gradient perpendicular to the flow direction (coming from the side towards the middle of the pipe). This calculation is performed changing mesh parameters, in particular:

- mesh grid: coarse, normal and extra fine.

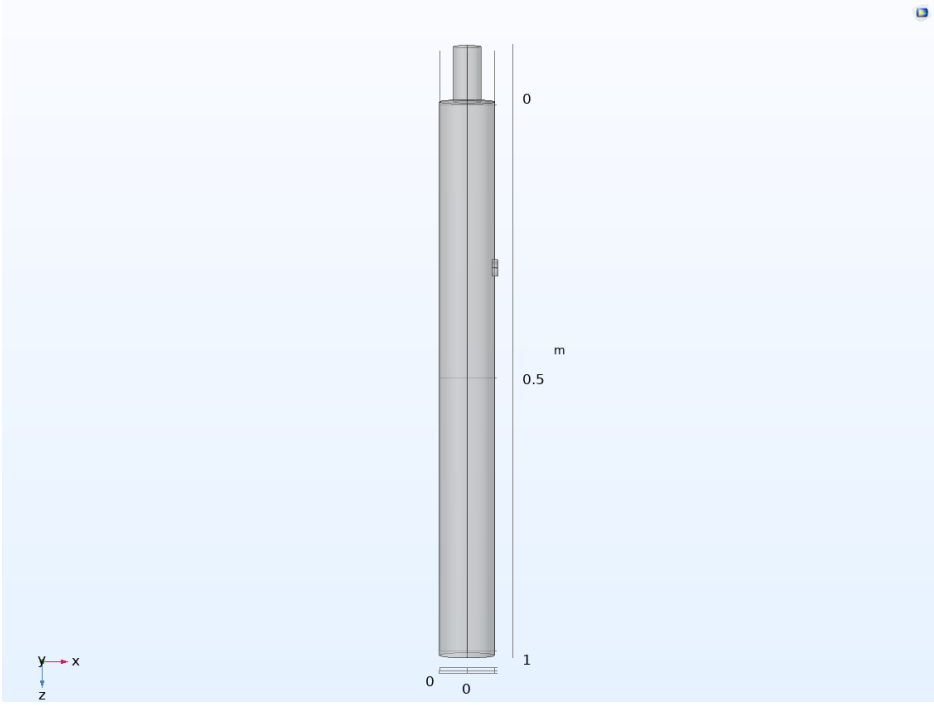

Figure 7: Numerical diffusion testing domain, side inlet in *further downstream* configuration

As for the normal mesh grid, the outcome is presented in Figure 8. Mass transport is evident, but the critical portion to look at is *just upstream* the side inlet. There, the final concentration of solute should be drastically lower, as it is naturally pushed in the direction of the flow. However, it should not be zero, as diffusion depends only on the spatial concentration gradient. It has nothing to do with the flow velocity field. Since the result is physically meaningful, the numerical diffusion is judged negligibly small.

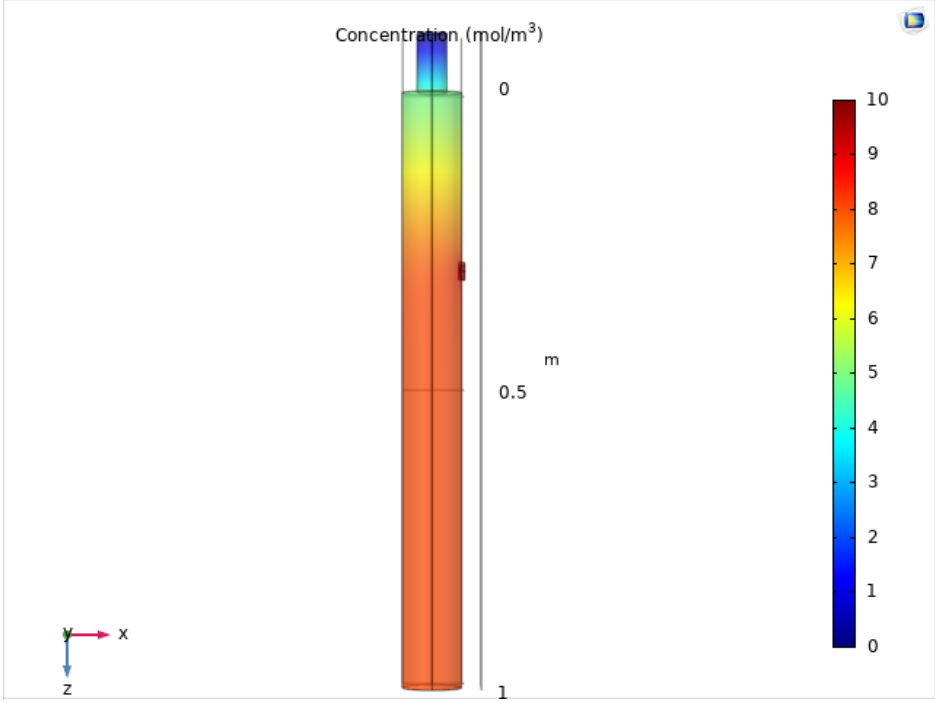

Figure 8: Outcome of numerical diffusion test: side inlet in *further downstream* configuration; mesh grid *normal*; $Re = 2500$, turbulent flow

As for the other two mesh cases (coarse and extra fine), the results are exactly equivalent to Figure 8.

4 Numerical Results

4.1 Model Choice

Due to the geometry of the pipe, the flow treated in this report was modelled with both laminar and turbulent solvers. Small inlet pipes (0.004 m in diameter) determine the injected flow to be turbulent. However, the main pipe has a much larger diameter (0.05 m), and the resulting Reynolds number (≈ 1700) is below transition (considered to be ≈ 2300). At first, the flow was computed using the stationary k-ε solver. Looking at the streamlines (see Figure 14), one can see complicated vortex structures upstream and downstream the slanted inlets.

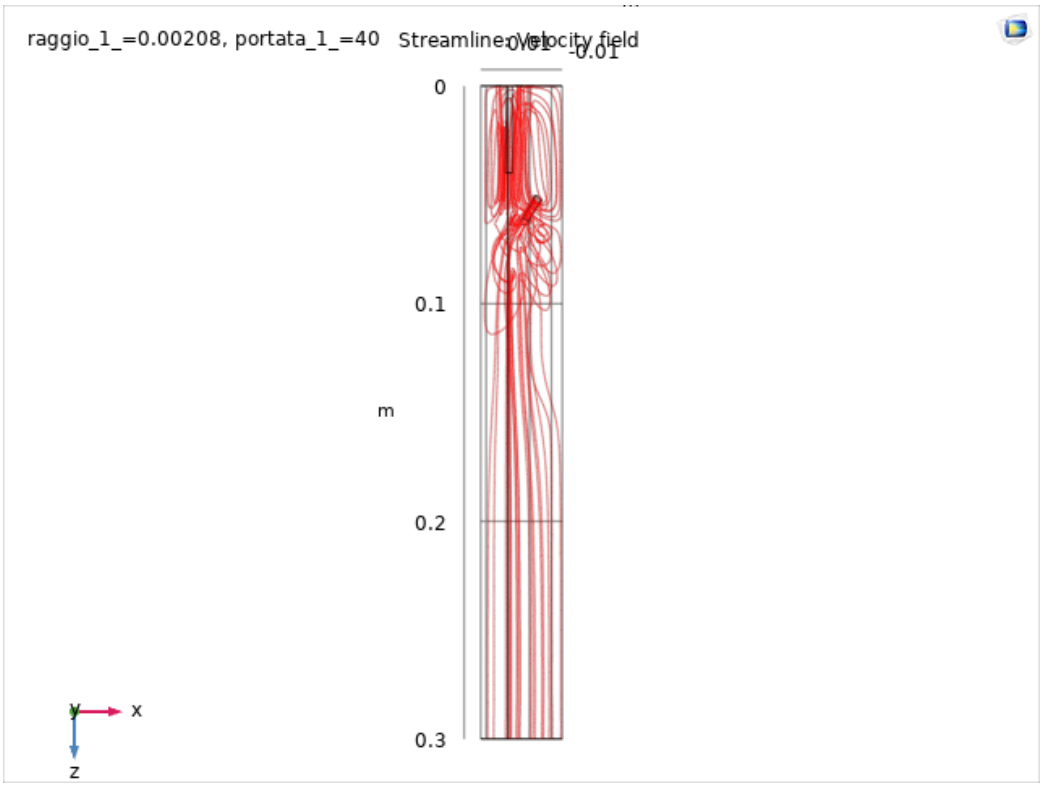

Figure 9: Turbulent flow streamlines. $k - \varepsilon$ model computation. Vortex structures are present upstream and downstream the slanted inlets

The flow structure in the main pipe is a *direct consequence* of the flow in the inlets, which is turbulent. The only effect of the local Reynolds number is the

relaminarization of the flow. This process is not at all immediate: the flow needs to run a few diameters before returning laminar. As mentioned in (*8*), a typical parameter in the study of dynamical systems is the perturbations half-life τ, indicating how long it takes for half of the initial perturbated states to decay. In (*15*), τ is shown to be proportional to:

$$\tau \propto (Re_c - Re_{loc}) = 50 \tag{59}$$

where the identified critical Reynolds number is $Re_c = 1750$ and the local Reynolds number 1700. As shown in Figure 10, when $Re_c = Re_{loc}$, the half life diverges. Its inverse, the *decay rate*, approaches zero:

$$\tau^{-1} \propto (Re_c - Re_{loc})^{-1} = 0.02 \tag{60}$$

For these reasons, the flow in the mixing chamber is modelled using a *turbulent solver*.

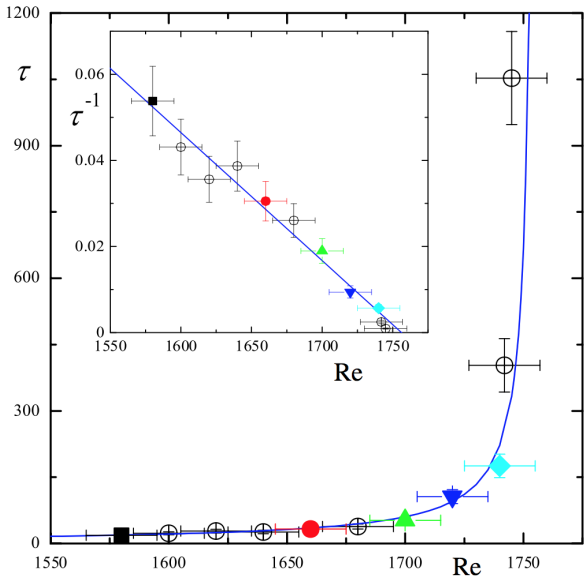

Figure 10: Half-life τ and decay rate τ^{-1} as a function of Re_{loc}. Colored dots correspond to experimental findings. Green dot coincides with treated case ($Re_{loc} = 1700$). Sharp cutoff at $Re_{loc} = 1750$. Source: (*15*)

4.2 k-ε

To ensure *reproducibility*, main options of k-ε simulations are listed below, together with the selected values. Readers have to bear in mind that all k-ϵ simulations are carried out exploiting the symmetry of the domain (considering only $\frac{1}{3}$ of the cross-section).

- Density: *From material* (air);
- Dynamic viscosity: *From material* (air);
- Wall condition: *no-slip*;
- Inlet, Boundary Condition: *Fully developed flow*, and then *Flow rate*;
- Particle diameter: *1 μm*;
- Outlet, Boundary Condition *Pressure*;

4.2.1 Results

The plots describing the velocity field obtained from the turbulent simulations are presented below. They consist of *velocity slices*, color plots slicing the domain and describing the velocity magnitude, and *streamlines*.

Figure 11 presents xy domain slices of the velocity field longitudinal component (z). Maximum values are reached about the slanted inlets, whereas in the rest of the domain the velocity is almost uniform. In the upper part of the pipe, the velocity increases in the central area (yellow) and decreases towards the wall (blue). Since this can be a sign of recirculation, both horizontal domain slices (yz) and streamlines are investigated.

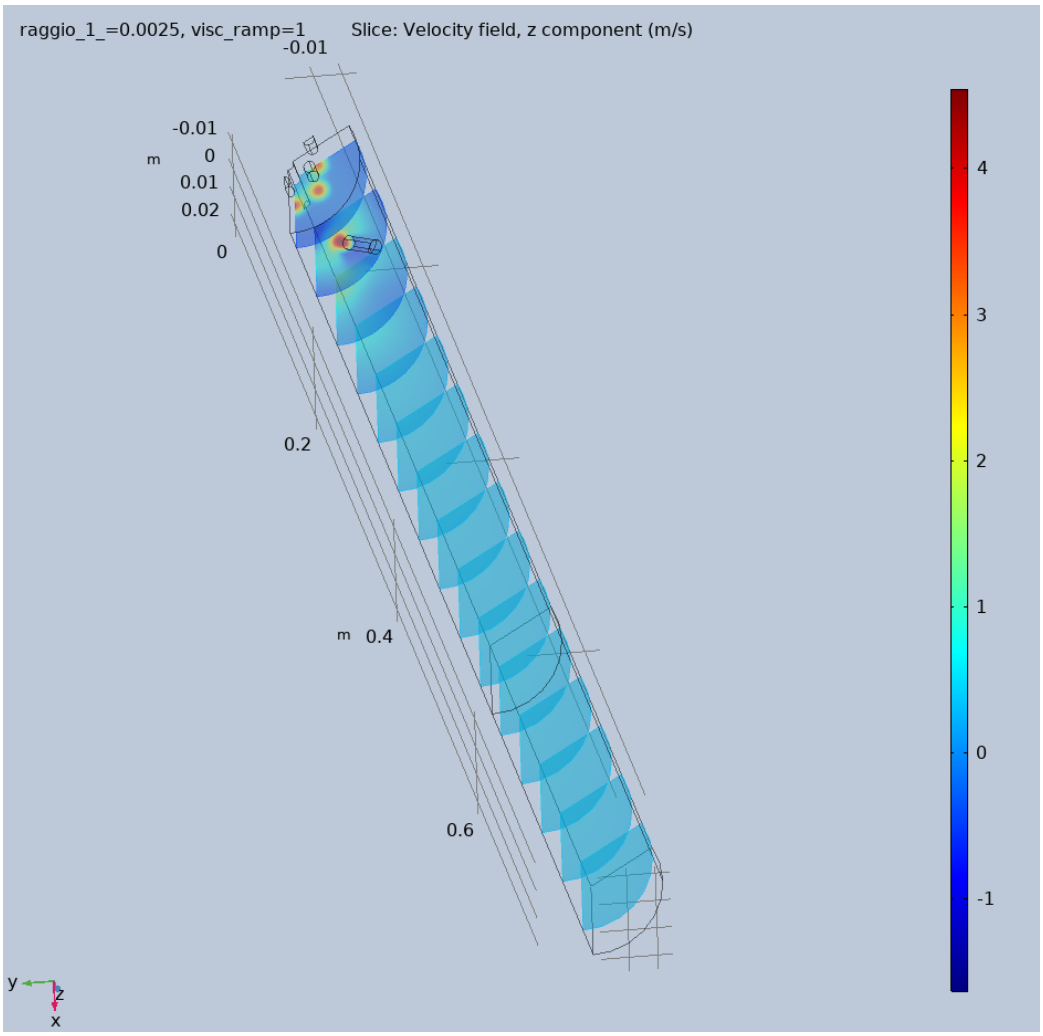

Figure 11: xy domain slices of the longitudinal component (z) of the velocity field

In the first 20 cm of the mixing chamber, the longitudinal speed in the central area is higher than close to the wall (see Figure 12 and 13). This is caused by the inlets, both those on the very top and those on the side. Close to all inlets, the velocity magnitude tops 4 m/s. This happens despite the one slanted inlet shown in Figure 13 does not lie on the domain slice.

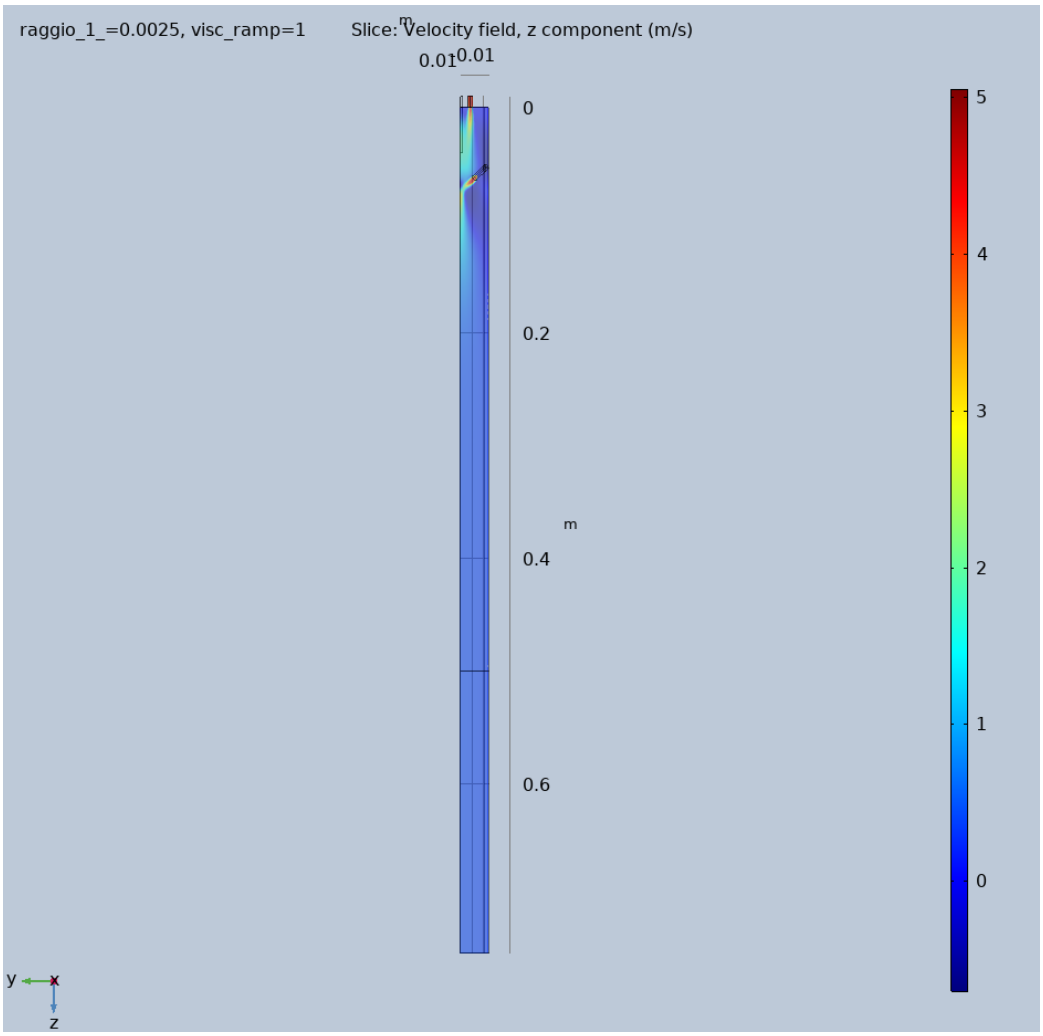

Figure 12: yz (horizontal) domain slices of the longitudinal component (z) of the velocity field

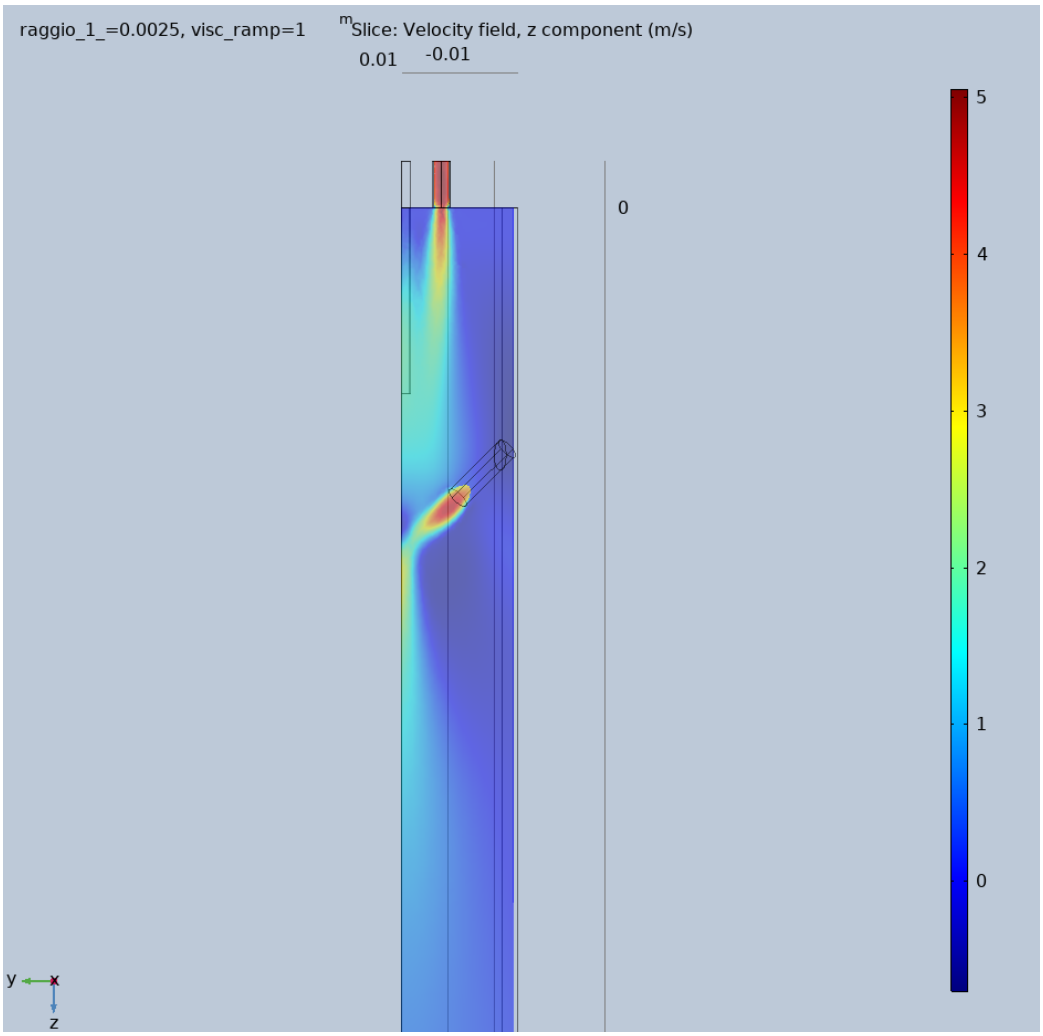

Figure 13: Zoom of Figure 12

In figure 14 streamlines confirm the presence of two recirculation zones, one upstream and one downstream the slanted inlets. The latter is much more complicated, as streamlines intersect often and do not lie on any of the fundamental planes (xy, yz, xz) of the mixing chamber. Moreover, the z component of the velocity field is not uniform when cutting the domain with an xy plane. It depends along which radius it is plotted. This is shown in Figure 15, where the 2 z-velocity functions refer to z=0.08 m. The blue function (in the legend referred to as *slanted inlet*) is plotted along the radius downstream the axis

of the slanted inlet. Instead, the radius of the green function (in the legend referred to as *60_ deg_ shift*) is rotated of 60 deg with respect to the previous one. Only the blue function goes below zero, whereas the green function's absolute minimum is about 0.5 m/s.

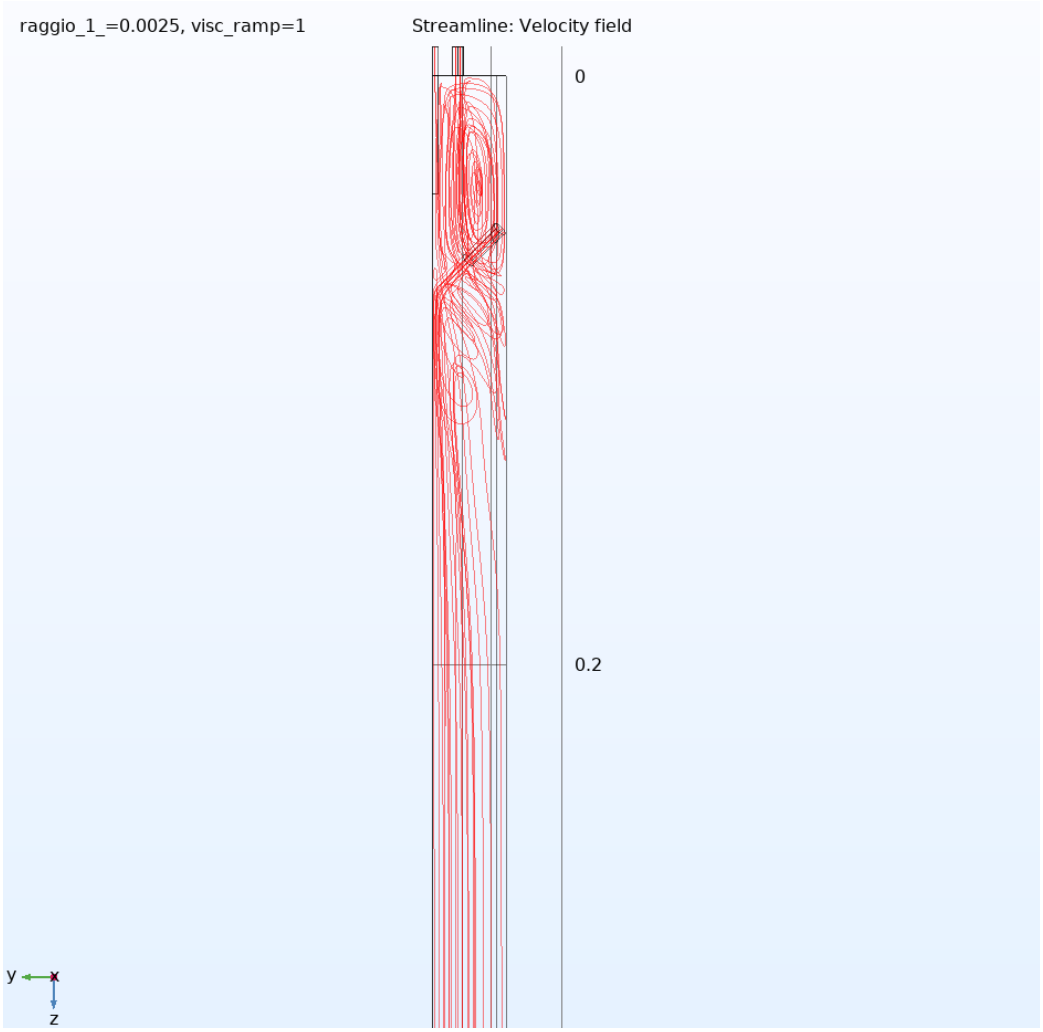

Figure 14: Streamlines showing two recirculations zones, upstream and downstream the slanted inlets. *Nota Bene:* further downstream (z $>$ 0.2 m), streamlines proceed straight.

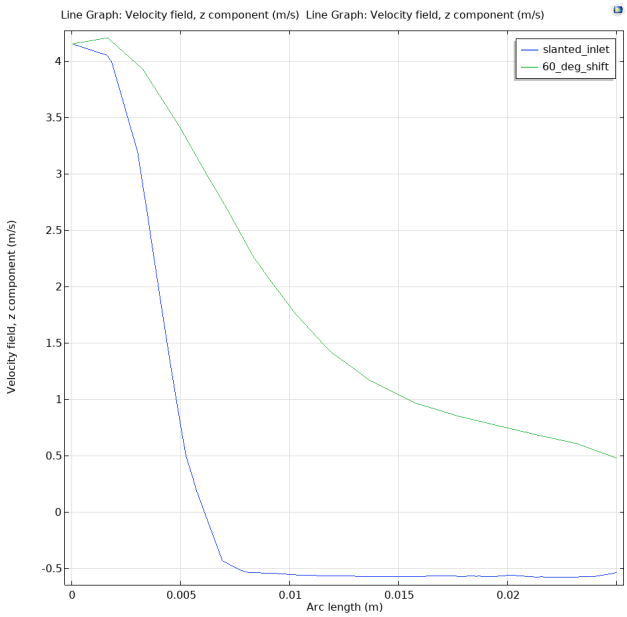

Figure 15: Two functions showing the z-component of the velocity field at z=0.08 m. Blue function is plotted along a radius lying below the slanted inlet, whereas the green line along a radius rotated 60 deg with respect to the previous one.

4.3 Particle Tracing for Fluid Flow

4.3.1 Configuration

To ensure *reproducibility*, main options of particle tracing simulations are listed below, together with the selected values. Readers have to bear in mind that all particle simulation are based on a k-ε solution, thus exploiting the same domain symmetry (only $\frac{1}{3}$ of the cross-section was considered).

- Formulation: *Newtonian*;
- Maximum number of secondary particles: *100000*. Secondary particles are those created after any original particle interaction, either wall-particle or particle-particle (in this case absent because of the very low volume fraction);
- Wall condition: *Bounce*, in order to simulate an elastic collision between particles and walls;

- Particle density: *2200 kg/m*^{2};
- Particle diameter: *1* μm;
- Initial position: *Density*, selecting 5000 particles per release;
- Drag law: *Stokes*, selecting velocity field from the k-ε solution;
- Turbulent dispersion: *Discrete random walk*, to model turbulent velocity field fluctuations; selecting the turbulent kinetic energy and dissipation rate from the k-ϵ solution. Furthermore, a Lagrangian time scale coefficient of $C_L = 0.2$ (see 3.3.2 or (*17*)) is picked.

Nota Bene: the *bounce* wall condition is rather unrealistic. Many particles stick to the wall. However, simulations consider fewer particles that those injected in the mixing chamber during experiments. Bouncing particles represent those which arrive to the end of mixing chamber and allow to draw conclusions related to concentration homogeneity. From here on, collisions between particles and the wall are addressed as *wall particle interactions*, or simply wall interactions.

4.3.2 Wall interactions

At first, no other parameters were investigated and particle trajectories were calculated for a 30 cm long infrastructure. Later on, the parameter called *Maximum number of wall interactions per time step* was edited. To visualize it, the *Advanced physics options* of the simulation must be enabled [5]. Its default value is equal to 1000, but this *is not enough* to properly model particle-wall interactions: there are many more particles hitting the wall per time step. Thus, if unchanged, this parameter would cause the *removal* of several particles and the result to be *inconsistent*. However, the Particle Tracing for Fluid Flow code in COMSOL is optimized only for the default value of such a parameter. When increasing it, computational cost rises severely. A brief analysis of the computational effort is presented in Figure 16. Here, the ordinate axis shows a *real time factor*, rather than a precise duration expressed in seconds. Although at a glance the latter option appears meaningful, it deeply depends on the used machine. Conversely, the real time

[5] Click on *File* - *Preferences* - *Show More Options* and, below *Physics*, make sure *Advanced physics options* is selected

factor does not. To draw the picture below, particle tracing simulations for a 15 cm long infrastructure are considered. It is the smallest domain portion ever considered in this project.

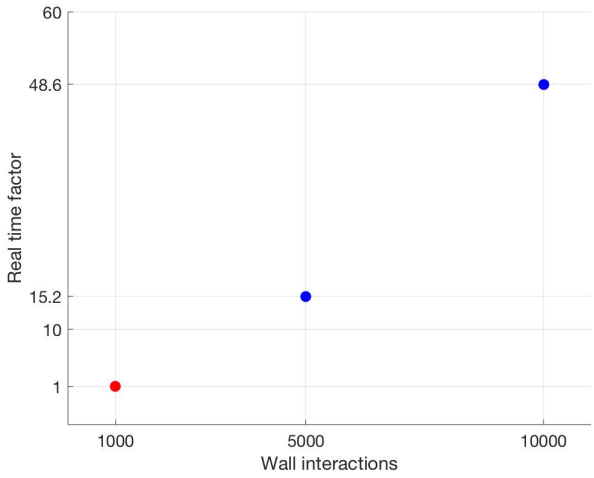

Figure 16: Real time factor concerning particle tracing simulations for a 15 cm long infrastructure

A clear non-linearity stands out. Reasons behind it are the following: when doubling such parameter, not only there are more particle-wall interactions to model, but going through the computation, more particles to solve for will be left. This is an unfortunate finding because it forces the author to run simulations without tracking all injected particles (as mentioned above, many of them are automatically removed). Indeed, the reference simulation (Figure 16, red dot) took about 3.5 hours to complete, and the longest more than a week. Furthermore, a simulation allowing 50000 particle-wall interactions per time step was run, but it has never been accomplished. After a while, the software simply stops the calculation. In conclusion, in this section COMSOL particle tracing results are discriminated against the allowed number of particle-wall interactions.

4.3.3 Accumulation Plots

Once particle trajectories have been determined, COMSOL displays them in the geometric domain (see Figure 17, in blue). Due to the high number

of involved particles, trajectories cannot be distinguished and further post-processing is necessary. By adding a so-called *accumulator* to the simulation outlet (coinciding with the outlet of the infrastructure), a virtual surface is created. It has the geometric properties (dimensions, position, ...) of the entity to which it is referred, and each particle hitting it leaves a footprint (Figures 18, 20, 21, 22 and 23, white dots). Moreover, it is possible to plot all 2D mesh elements (Figures listed just above, small black triangles) lying on the virtual surface and group them in large triangles. These big polygons are painted according to the number of particles hitting them. So, a qualitative measurement of concentration homogeneity is available.

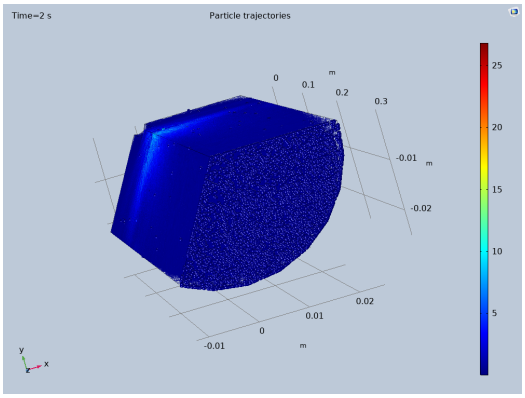

Figure 17: Example of particle trajectories plot. No post-processing required.

4.3.4 Accumulation vs Concentration

The above subsection outlines the advantages of accumulation plots, describing them as qualitative measurement of *concentration homogeneity*. On the other hand, one might argue that particle footprints are time independent, meaning they are permanent and there is no way to understand when a particle hit the surface. Conversely, concentration is a quantity referred to a single time instant: it should consider all particles present at that time in a given volume. Therefore, the possibility accumulation plots are misleading exists. Let's make a paradoxical example reflecting on two consecutive time instants. During the former, all particles hit one side of the virtual surface, and during the latter, the opposite. This way, heterogeneous concentrations follow each other in time, but when averaged, a much homogeneous concentration will appear. The reason why this possibility is discarded is twofold:

1. Firstly, concentration is a property evaluated out of a *volume*. Thus, for the previous example to become true, the two time steps should be well separated. However, all particles are injected at the same time. Thus, there is no reason why they should hit the virtual surface in so different time instants and, most of all, show such different patterns. Moreover, being the particle size uniform, they share equal relaxation time. In conclusion, they follow the flow in the same way.

2. Secondly, the turbulent regime attended by the flow is stationary. As a consequence, average velocity values found by solving the RANS equations do not vary in time. It is then impossible that only velocity fluctuations impose such drastic changes in the flow structure to determine completely different concentration in relatively consecutive time instants.

Despite these arguments are close to each other, they can be stated independently. In addition, now it is evident how local velocity fluctuations (which generate dispersion) are the only element differentiating particle trajectories.

Results

The accumulation plot describing the concentration 30 cm down the infrastructure is presented in Figure 18. In the simulation, only few particles can be tracked this far and hit the virtual surface. Two higher concentrations triangles (dark red) are spotted: the former in the central zone (corresponding to the top left corner of the plot) and the latter on the left. This last triangle lies in between two slanted inlets and can be identified by rotating 60 degrees from both of them (in Figure 3 one can see that the axes of the slanted inlets draw 120 degree angles). Moreover, particles are present in every part of the cross section, even the border (bottom right).

In conclusion, despite the low number of tracked particles, the concentration appears *fairly homogeneous*. The presence of the slanted inlets may cause the creation of a higher concentration zone, shifted 60 degrees in between them.

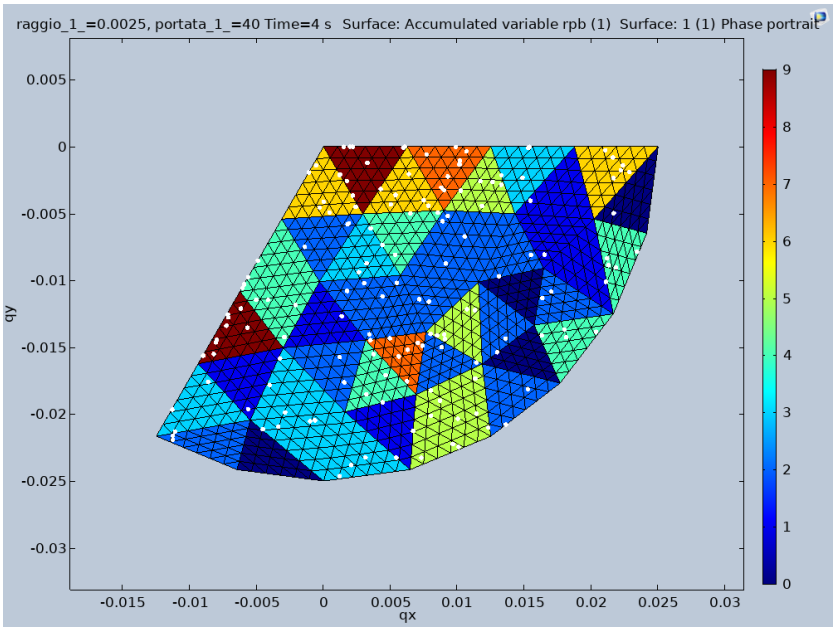

Figure 18: Accumulation plot, z=0.30m, radius of slanted inlets: 0.0025m, flow rate: 60L/min, wall-particle interactions: 1000

Streamlines in Figure 19 reveal that turbulent vortexes are located upstream $z = 0.20$m. A major recirculation zone lies upstream $z = 0.15$m. In addition, following the flow further downstream, one notices that the streamlines become straight. To study their influence, particle concentrations at $z = 0.15$m, $z = 0.17$m and $z = 0.20$m are investigated. This is a valid approach to understand how the last portion of the mixing flow works: is it still crucial or is it negligible? Because of the straight streamlines, the author believes downstream $z = 0.30$m, turbulent dispersion will be minimal. If so, the accumulation plot drawn at $z = 0.20$m should be similar to the one drawn at $z = 0.30$m.

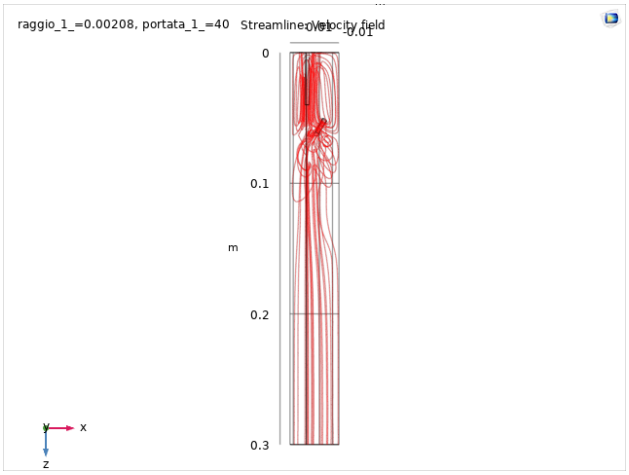

Figure 19: k-ϵ simulated streamlines in the 30cm infrastructure, flow rate: 60 L/min

Figure 20 shows the accumulation plot corresponding to $z = 0.15$m. It features many particles, most of them lying in the central portion of the flow (corresponding to the top left corner of the plot). The triangle which is hit by the largest number of particles (dark red) features almost 20 of them. Moving towards the wall, few dots are spotted and fewer than ten are encountered in large triangles adjacent to the boundary. Furthermore, a particle is found outside the 120-degree cross-section slice and is pointed at by a *red arrow*. This is because it ended up in one of the slanted inlets (here not visible). Finally, this plot testifies how particle concentration at $z = 0.15$m is strongly heterogeneous and reminds of the particle injection point: the center of the cross-section.

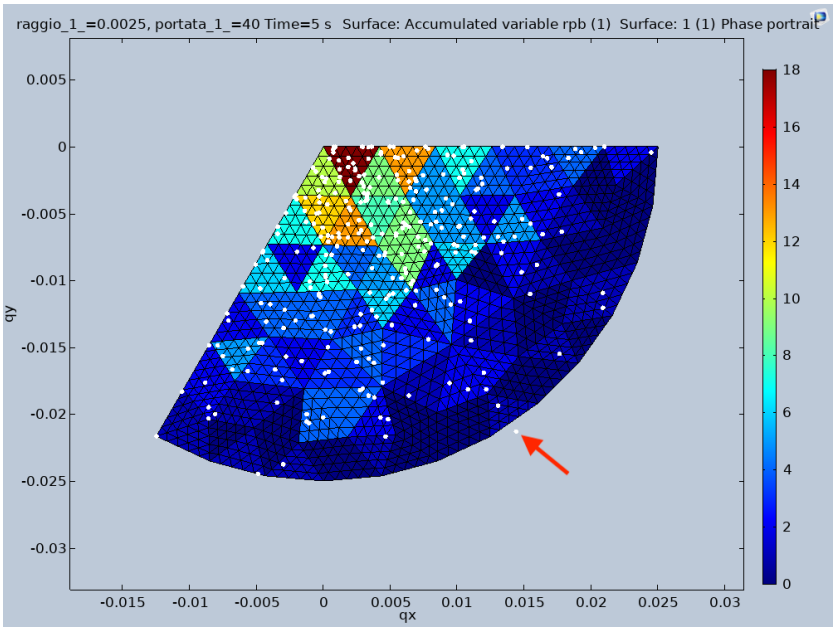

Figure 20: Accumulation plot, z=0.15m, radius of slanted inlets: 0.0025m, flow rate: 60L/min, wall-particle interactions: 1000

Particle concentration at $z = 0.15$m is also investigated by setting the number of allowed wall interactions to 5000 (thus 5 times the default value). The resulting plot is presented in Figure 21. The overall conclusion does not change, as particles occupy mostly the inner zone of the domain (corresponding to the top left corner of the plot). The main difference with respect to Figure 20 lies in the number of displayed dots, here much greater. Indeed, the middle part of the domain features several red triangles, even if in this case, dark red corresponds to 17 particles instead of 18. Finally, dots found in the slanted inlets (outside the 120-degree cross-section slice) are 5 instead of 1.

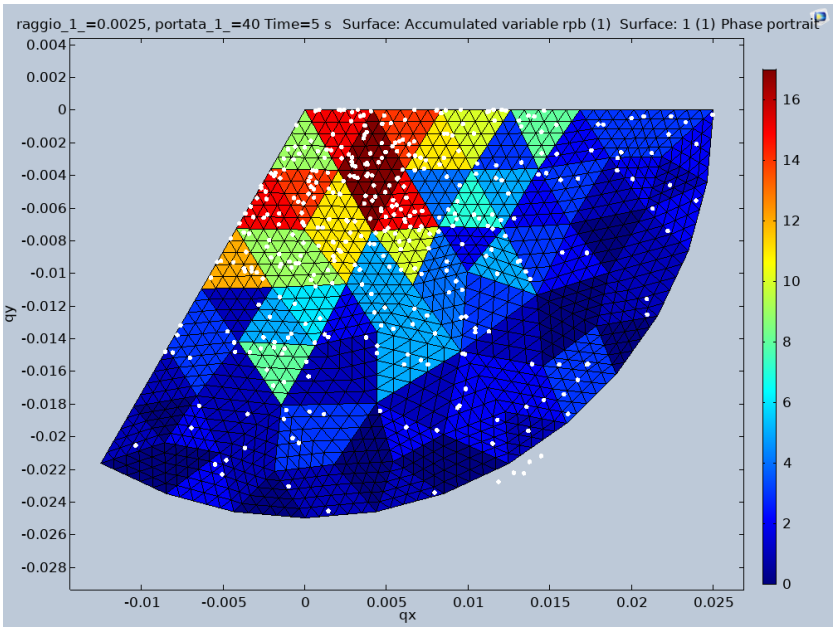

Figure 21: Accumulation plot, z=0.15m, radius of slanted inlets: 0.0025m, flow rate: 60L/min, wall-particle interactions: 5000

Figure 22 shows the accumulation plot corresponding to $z = 0.17$m. It features far less dots than the previous two plots: in this case, dark red triangles are hit by only 11 particles. On the other hand, concentration seems much more homogeneous, even if it still presents a peak in the central area (corresponding to the top left corner of the plot). Moving along the wall, one encounters few particles. In addition, no dots are found outside the cross-section (corresponding to the slanted inlets). On the contrary, the area between two of the slanted inlets (found by rotating 60 degrees from one towards the other and corresponding to the bottom left portion of the plot) has more particles than before. This portion of the cross-section resembles more the Figure 18.

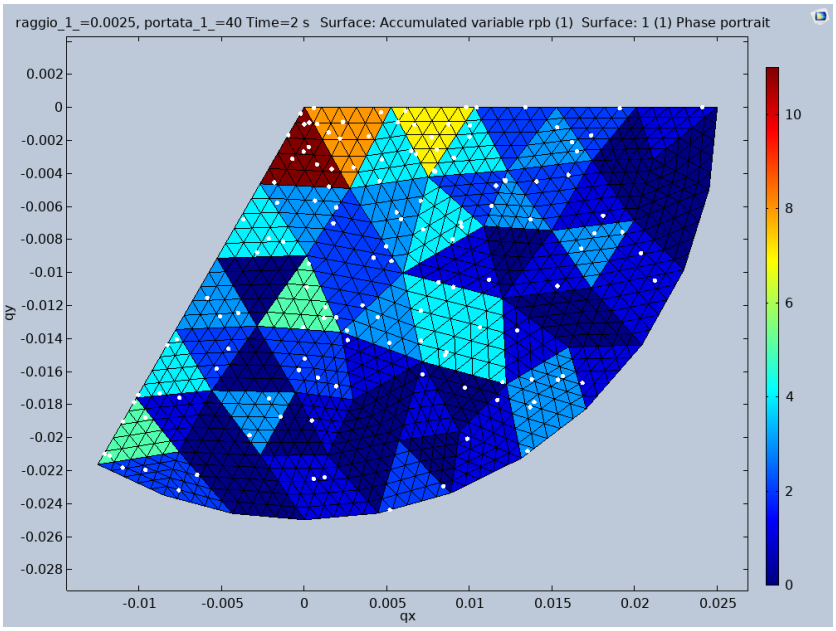

Figure 22: Accumulation plot, z=0.17m, radius of slanted inlets: 0.0025m, flow rate: 60L/min, wall-particle interactions: 1000

Proceeding downstream the flow, the accumulation plot corresponding to $z =$ 0.20m is shown in Figure 23. Again, few particles are present. Concentration improvements with respect to Figure 22 are evident: particles are present in almost every portion of the plot and dark red triangles are hit only 7 times. As before, many particles are found in the area between the two slanted inlets (found by rotating 60 degrees from one towards the other and corresponding to the bottom left portion of the plot). Finally, no particles are found outside the cross-section in the slanted inlets. This last fact might be a matter of randomness.

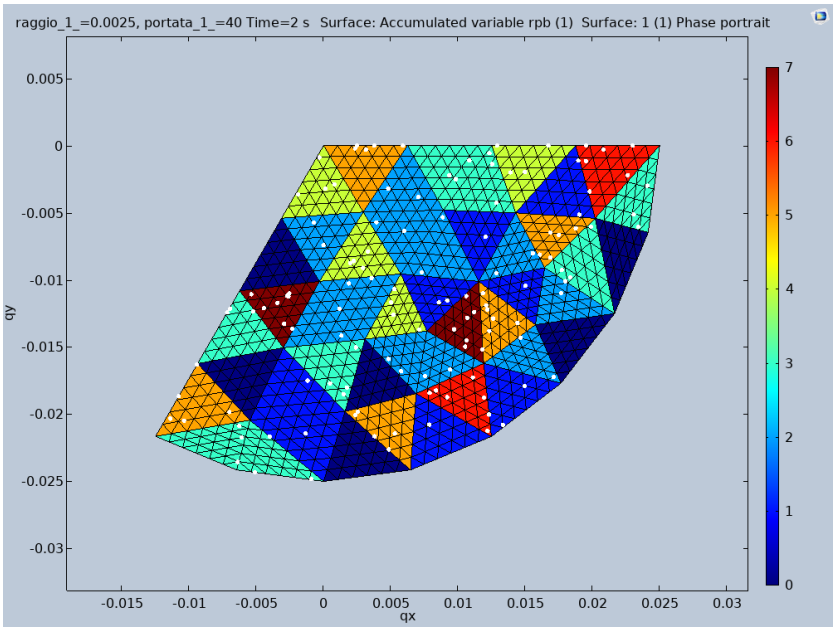

Figure 23: Accumulation plot, z=0.20m, radius of slanted inlets: 0.0025m, flow rate: 60L/min, wall-particle interactions: 1000

Even if this plot is related to the virtual surface only 3 cm downstream the previous, their differences are large. Indeed, it resembles Figure 18, which is referred to $z = 0.30$m, more than *3 times further away* than Figure 22.

In conclusion, concentration homogeneity largely improves starting from $z = 0.20$m, confirming what stated above about the streamlines. On the other hand, plots referred to $z = 0.17$m, $z = 0.20$m and $z = 0.30$m feature a drastic decrease in tracked particles. This clearly affects both their *reliability* and *reproducibility*, because one cannot be sure whether the statistics is already matched.

Particle Removal

As mentioned above, only a given value of wall-particle interactions per time step are allowed. In all discussed simulations, 5000 particles are injected. Each time step, when the number of allowed wall interactions is reached, remaining particles hitting the wall are removed. When this value is increased to 5000, more particle reach the end of the infrastructure. This is clear when

comparing Figure 20 and Figure 21. However, when the allowed wall interactions are further raised, particles reaching the end are decrease. Moreover, if the wall interactions parameter were the only limiting factor, it should always be smaller (or equal) than the number of particles present on any accumulation plots. Clearly, in Figure 20 there are less than 1000 particles. Thus, the previous assumption is disproved. In addition, when running the same simulation allowing for 10000 particle-wall interactions, less particles than in any other cases are tracked.
To further investigate this aspect and find the other limiting factor, another simulation has been run. This time, particles have 10 times the previous diameter (original diameter $d_p = 1\mu$m). As shown in Figure 24, thousands of them reach the virtual surface.

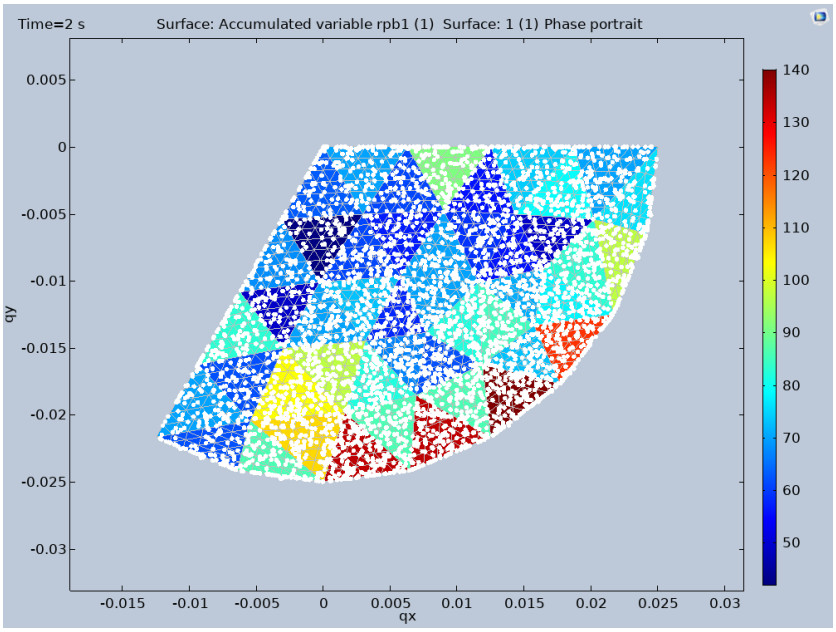

Figure 24: Accumulation plot, z=0.30m, particle diameter: 1μm, flow rate: 60L/min, wall-particle interactions: 1000

It is now clear that the limiting factor is somehow related to the size of the particle. According to equation 52, the particle relaxation time is quadratically proportional to its diameter. Thus, 1μm sized-particles have a 100 times smaller relaxation times, and tend to follow the flow much better. When approaching the wall, these particles are subject to the steep gradients caused

by the boundary layer (in case of the k-ε coupling, the latter is simulated using wall functions) and therefore a very small time step is needed to solve for their positions. Probably, this time step becomes so small that particles simply cannot be tracked and have to be removed from the simulation.

4.4 Transport of Diluted Species

4.4.1 Configuration

To ensure *reproducibility*, main options of transport of diluted species simulations are listed below, together with the selected values.

- Velocity field: solution of k-ϵ model;
- Diffusion coefficient: user defined, selecting $D = 10^{-10} m^2/s$.
- Initial values (solute concentration in the domain): $c1 = 0 mol/m^3$;
- Inflow: top set to $c = 0 mol/m^3$, side set to $c = 10 mol/m^3$;
- Transport Properties: turbulent mixing, selecting the turbulent kinematic viscosity from the k-ϵ solution and selecting a turbulent Schmidt number $S_{CT} = 0.7$.

4.4.2 Results

The obtained solute concentration is presented in the figures below. A qualitative graph revealing the solute concentration on the mixing chamber inner surface is shown in Figure 25. Another qualitative plot is introduced in Figure 27, where the concentration is displayed on 15 domain slices. Respective zooms follow each picture (Figure 26 and Figure 28).

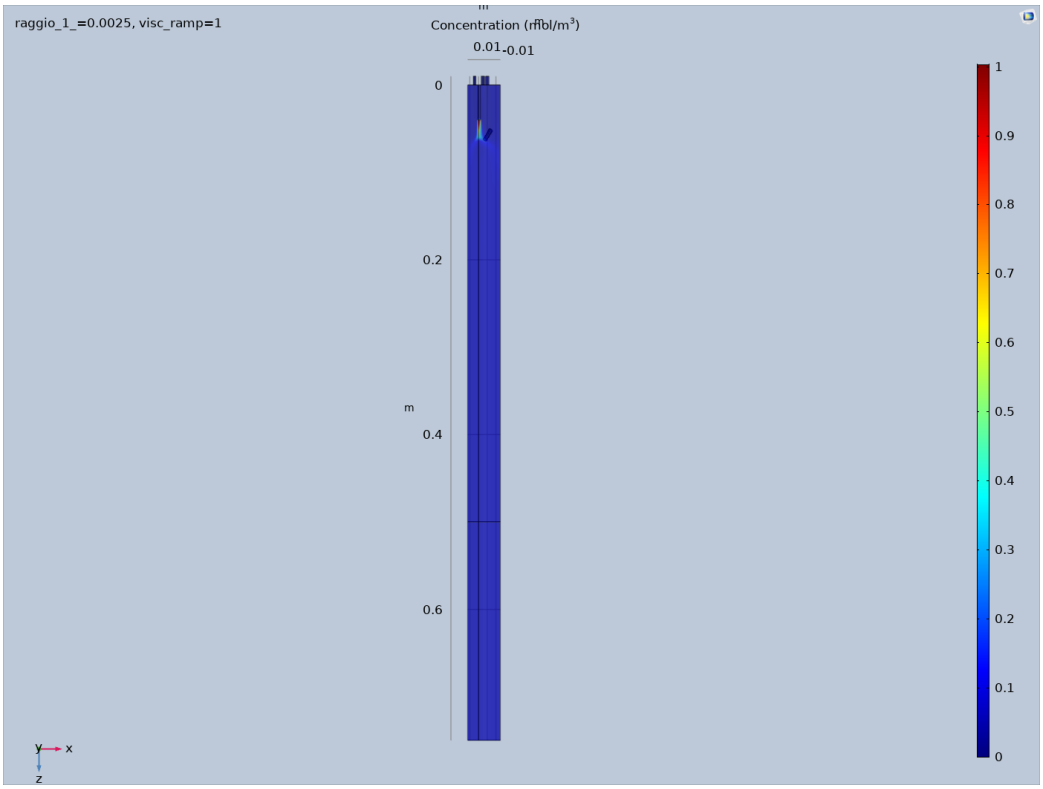

Figure 25: Concentration plot, solute concentration on the mixing chamber inner surface

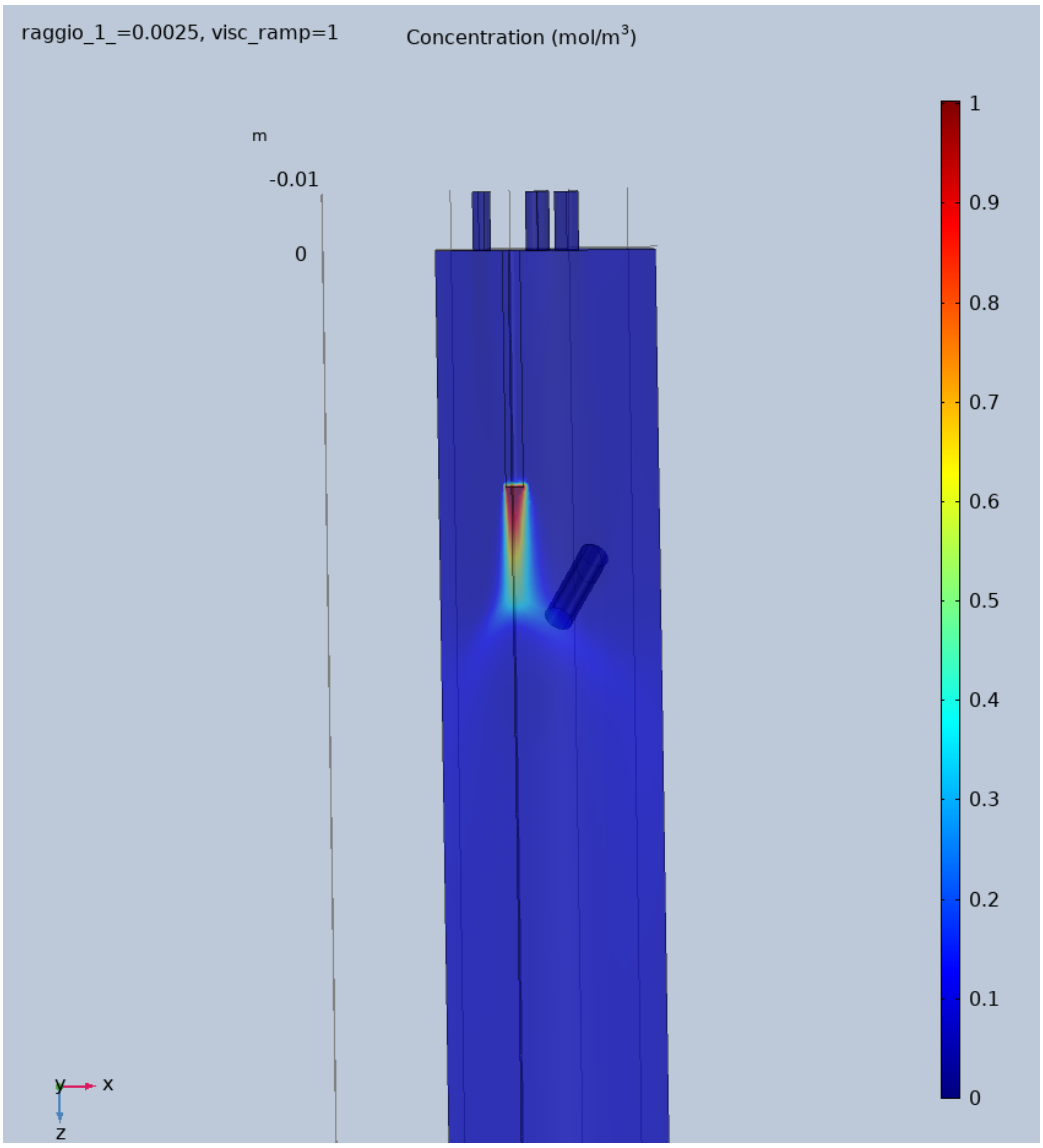

Figure 26: Concentration plot, zoom of Figure 25 on central inlet

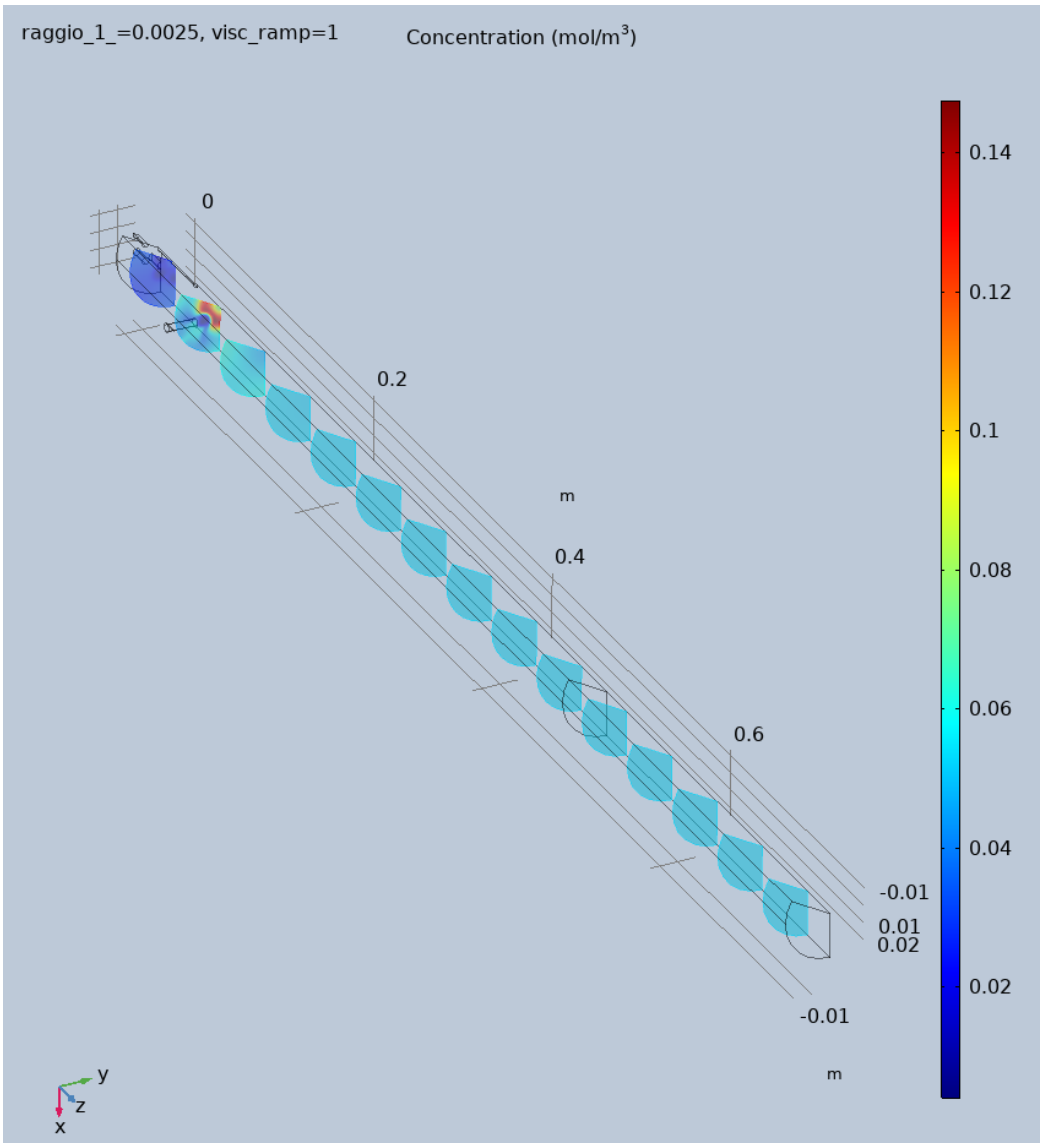

Figure 27: Concentration plot, 15 xy slices of concentration

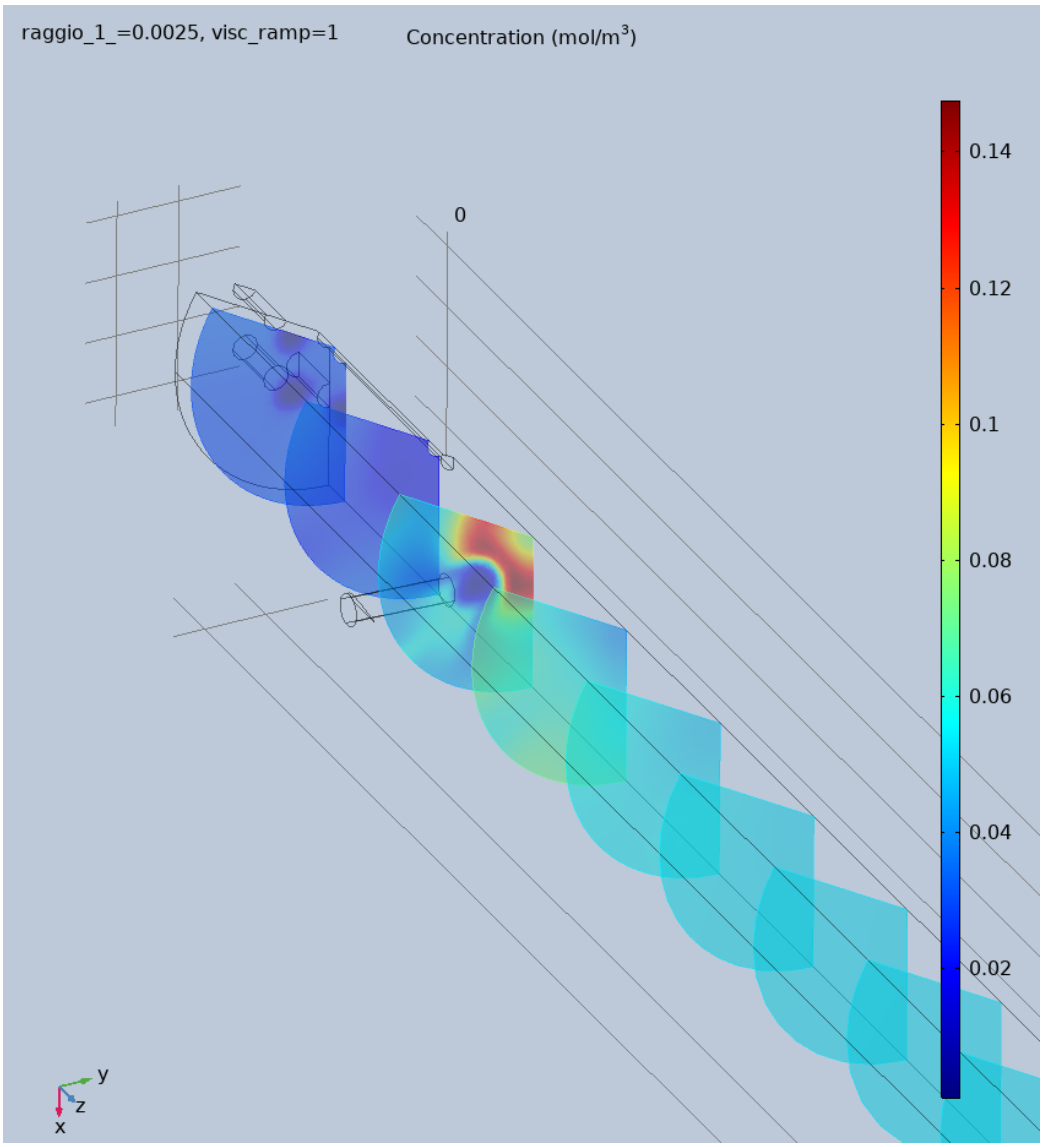

Figure 28: Concentration plot, zoom of Figure 27 on central inlet

Not only these figures allow to assess the situation concerning the concentration homogeneity, but also to determine the most heterogeneous areas of any cross sections. As for the bottom part of the mixing chamber, it is necessary to change the coloring range to 0.0526 - 0.0527 mol/m^3 to spot heterogeneity. It then corresponds to the portion beneath the slanted inlets (see Figure 29,

around the red line). To evaluate the worst scenario, quantitative graphs will be referred to those areas. More in detail, the solute concentration chosen along the just shown red line is plotted in Figure 30. Also, the homogeneity is measured by plotting the ratio of the concentration along the red line to the concentration in the centre of the chamber ($R = 0$ m). The homogeneity accuracy is very high, as the ratio plot is almost flat.
In addition, outcomes show the same concentration homogeneity even upstream the outlet. Significant concentration heterogeneity (larger than 1%, or more precisely, 0.953%), is spotted *upstream* of z=0.20 m.

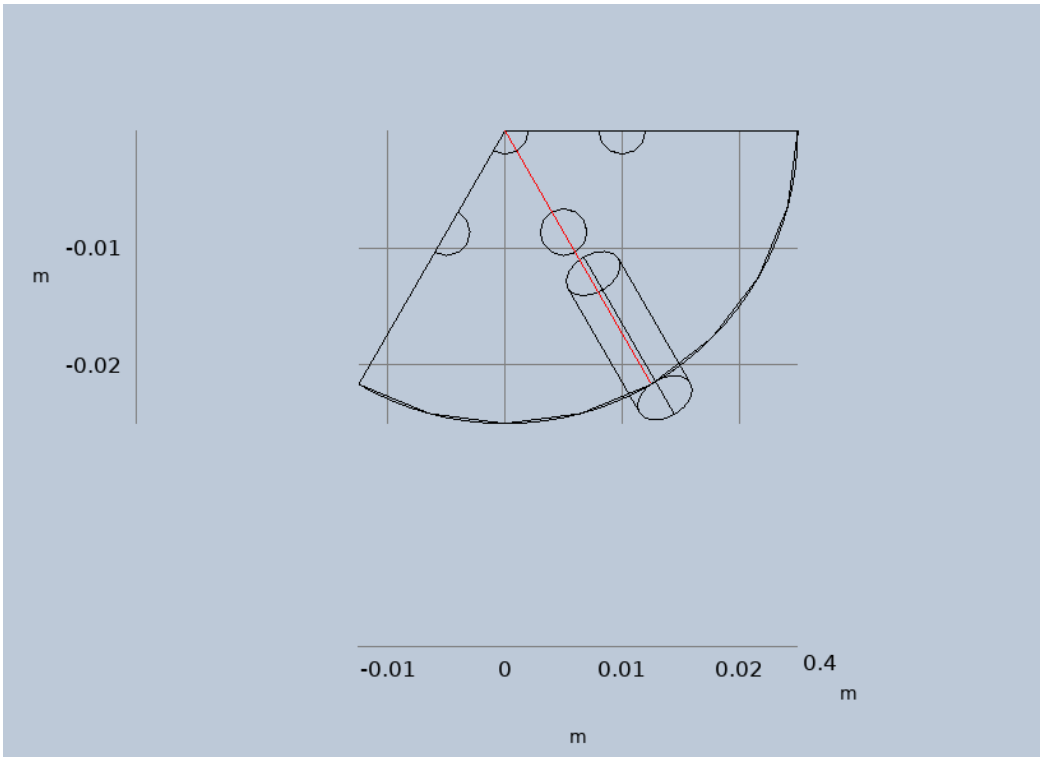

Figure 29: Top view of $\frac{1}{3}$ of the mixing chamber showing line along which concentration plots refer to (in red)

To confirm how crucial the small eddies are for the mixing (see subsection 3.3.3), a *Transport of Diluted Species* simulation omitting the term $\frac{\nu_T}{Sc_T}$ is performed. Its outcome is presented in Figure 31: concentration homogeneity is *far less* accurate than before.

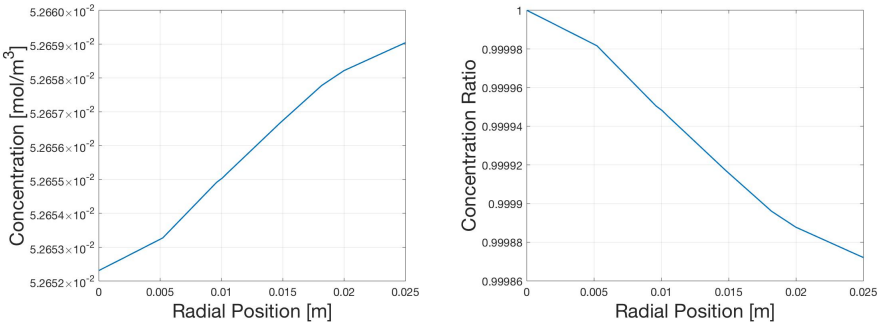

Figure 30: Left: concentration plot of simulation allowing turbulent dispersion: z=0.70m, along red line in Figure 29.
Right: ratio of concentration along red line to concentration in the centre (R = 0 m)

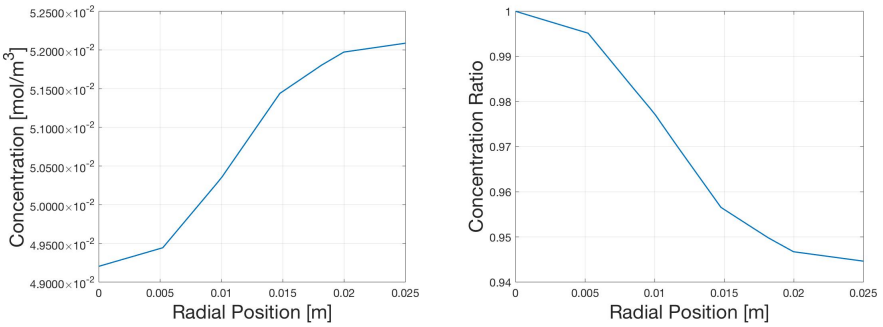

Figure 31: Left: concentration plot of sim. *without* turbulent dispersion: z=0.70m, along red line in Figure 29.
Right: ratio of concentration along red line to concentration in the centre (R = 0 m)

5 Experimental Results

5.1 Equipment

The equipment used to perform the experiments consists of a pressure reducer, two mass flow controllers, two Condensation Particle Counters (CPCs), an atomizer, and a computer. The whole infrastructure is sketched in Figure 32.

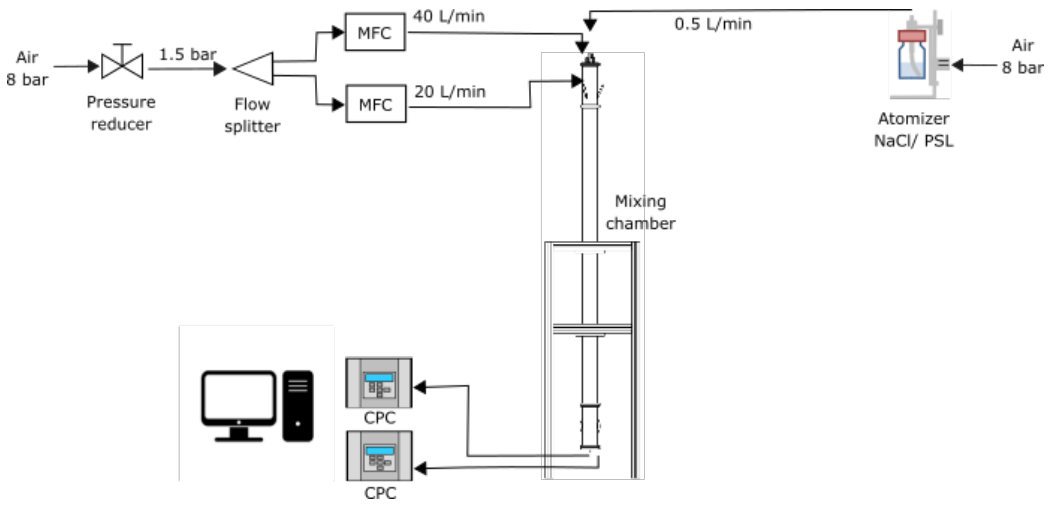

Figure 32: Sketch of the experimental setup: pressure reducer, mass flow controllers (2), mixing chamber, atomizer, Condensation Particle Counter (CPCs) (2), computer

The pressure reducer is simply a manometer used to diminish the pressure of the outcoming airflow, set at 1.5 bar. It is connected to the lab pressurized airflow generator, which releases air with a pressure of 8 bar.
The mass flow controllers allow to set a desired mass flow and keep it constant in time. They work as follows: the incoming airflow enters the device and splits into the sensor pipe and the bypass. The flow rate through the sensor pipe is measured by a sensor which evaluates the temperature variation in the duct. This variation is converted into an electric signal and compared to the set flow rate. The difference between the two is computed and the valve at the outlet of the device is regulated consequently. Moreover, the flow in the bypass pipe merges the one in the sensor pipe upstream the valve. The model used is ALICAT MCR-50SLPM-D/5M.

The CPCs count aerosol particles through laser scattering. Since they would not be able to detect particles below 1μm, they are first nucleated through thermal diffusion (here the name *condensation*) (*36*). To do so, CPCs employ butanol, which is constantly supplied. The models used are Grimm 5.412 and TSI 3775.
The atomizer exploits Bernoulli's theorem to vaporize a mixture of water and a solute and let it in the airflow. To evaluate different particle size distributions, both salt ($NaCl$) and polystyrene latex (PSL) were employed as solutes (peaks of 80 nm and 900 nm respectively).
Finally, two probes are used to sample the flow. They consist in 2 identical steel pipes with a diameter of 4 mm. They are inserted in small holes at the bottom of the mixing chamber and connected to pipes leading to the CPCs. They are long enough to sample the flow upstream the exhaust of the chamber.

5.2 Process Explanation

The experiment is performed as follows. First, CPCs and mass flow controllers are started and brought up to speed. This takes approximately half an hour. In the meantime, the solution of water and salt or water and PSL is prepared. In case of PSL, the solution has to undergo *ultrasonication*: it is placed in a small basin and irradiated with ultrasounds. This is to destroy eventual *particle agglomerates*. The final solution is then placed in a becher and mounted on the atomizer. The salt/PSL solution is vaporized and injected in the central inlet, on the very top of the mixing chamber. The flow rate is small, only 0.5 L/min. The other six inlets on the very top deliver (in total) 40 L/min of pure air and the three on the side 20 L/min (in total).
When the infrastructure is ready, the sampling process begins. The two probes are inserted in the holes at the very bottom of the mixing chamber. One of them is always placed in the middle, whereas the other one in a random position. Aerosol particles are now flowing from the probes to the two CPCs inlets, where particles are counted once per second. The two probes have equal length, thus sample flow at a fixed longitudinal coordinate in the mixing chamber. Moreover, for the entire duration of the sampling, the two probes are held in position by some tape or small screws. Each sampling operation lasts 60 seconds. 60 measurements are performed (1 per second) and their average is selected as the final concentration value. The data are recorded on the computer and saved on an Excel sheet. Later, the position

of the second probe is changed to another of the 8 holes (9 when counting the one in the middle) and the process is repeated.

To assess concentration homogeneity, the concentration in a general point at the outlet of the chamber is divided by the concentration in the centre. Since two CPCs are needed, systematic uncertainty of each one of them must be taken into account when processing the raw data. More in detail, CPCs present an efficiency ε and a calibration uncertainty c_u. Thus, concentration homogeneity C_H is evaluated as:

$$C_H = \frac{\frac{C_g}{\varepsilon_g}}{\frac{C_c}{\varepsilon_c}} \pm c_u = \frac{C_g \varepsilon_c}{C_c \varepsilon_g} \pm c_u \tag{61}$$

where C_g and C_c represent the number of particles sampled by the two CPCs respectively in a general position and at the centre.
As for the CPCs used, their efficiency is close to one and their calibration uncertainty is 3%. Therefore,

$$c_u = \sqrt{0.03^2 + 0.03^2} = 0.03 \cdot \sqrt{2} = 0.0424 \tag{62}$$

5.3 Results

Results are presented in the following plots. As mentioned before, the homogeneity target interval ranges from 0.95 to 1.05.

In Figure 33, concentration homogeneities of salt and PSL particles are presented. The former show a smaller deviation from the unity ratio, and they are all off of approximately 2%. Furthermore, their error bars are almost completely in the target range. Instead, the latter have a larger and heterogeneous deviation. Moreover, PLS concentration on the sides is 5% off the unit value. This, without considering the error bars.

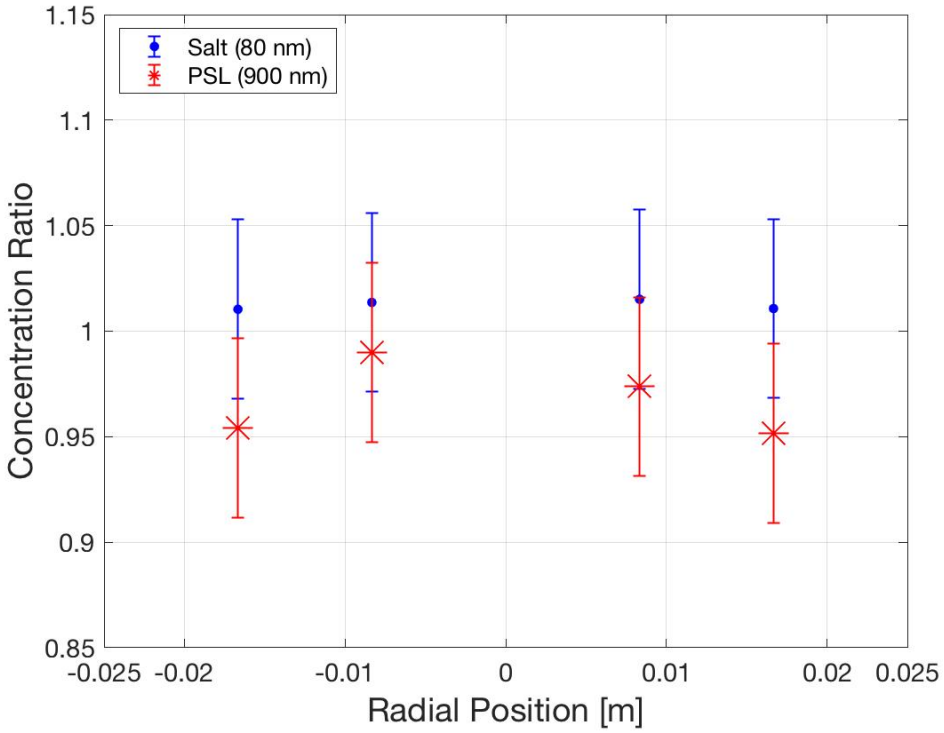

Figure 33: Salt and PSL concentration homogeneity

The reason behind this large difference in homogeneity is the *relaxation time*, thus how soon do the particles tend to follow the flow. This quantity is directly proportional to the particle density, but quadratically proportional to their diameter (see equation 52). As mentioned in subsection 5.1, particle size peaks of salt and PSL vary of one order of magnitude in favour of PSL. Instead, the density of salt is only 1.5 times higher than the one of PSL ($\rho_{NaCl} \approx 2100$ kg/m^3, $\rho_{PSL} \approx 1050$ kg/m^3). Therefore, the relaxation time of PSL particles is almost two orders of magnitude higher than the one of salt. More precisely,

$$\frac{\tau_{PSL}}{\tau_{NaCl}} = \frac{d_{PSL}^2 \rho_{PSL}}{18\mu} \cdot \frac{18\mu}{d_{NaCl}^2 \rho_{NaCl}} = \frac{d_{PSL}^2 \rho_{PSL}}{d_{NaCl}^2 \rho_{NaCl}} = 63.2 \tag{63}$$

In conclusion, salt particles are prone to follow the fluid and thus exploit *turbulent dispersion*, which in subsection 4.4.2 has been proved to be the dominant mixing mechanism.

To address the research question *how much can the flow rates be reduced without affecting the concentration homogeneity at the outlet?*, the experiment was repeated with:

1. half flow rates: 20 L/min from top and 10 L/min from the sides;
2. equal flow rates: 10 L/min from top and 10 L/min from the sides;

The flow rate of 0.5 L/min coming from the top central inlet (the one where particles are injected) is never changed. As for salt, new configurations are compared to the original one in Figure 34.

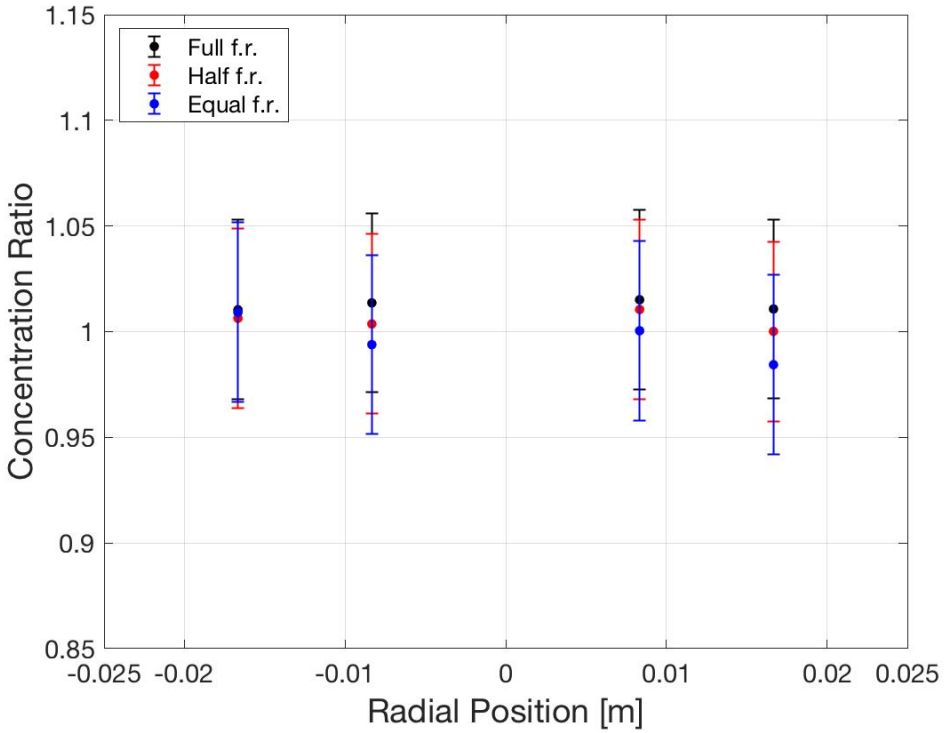

Figure 34: Flow rate reduction using salt particles: comparison

In Figure 34, no significant changes in the concentration homogeneity can be observed. Looking at the plot, one can see that with half flow rates and equal flow rates, salt particles perform slightly better. As a conclusion, salt

particles are not affected by reduces flow rates. They maintain a 2% biased homogeneous concentration along the entire diameter of the chamber.

To address the research question *how much can the mixing chamber length be further reduced without affecting the concentration homogeneity at the outlet?*, the salt particles experiment was repeated using a *shorter chamber*. Here, the modular structure explained in subsection 2.1 was exploited and the central component removed. As a result, there are now 0.57 m from the very top inlets and the sampling point. In Figure 35, the comparison between normal, reduced and equal flow rates is performed on the shorter mixing chamber.

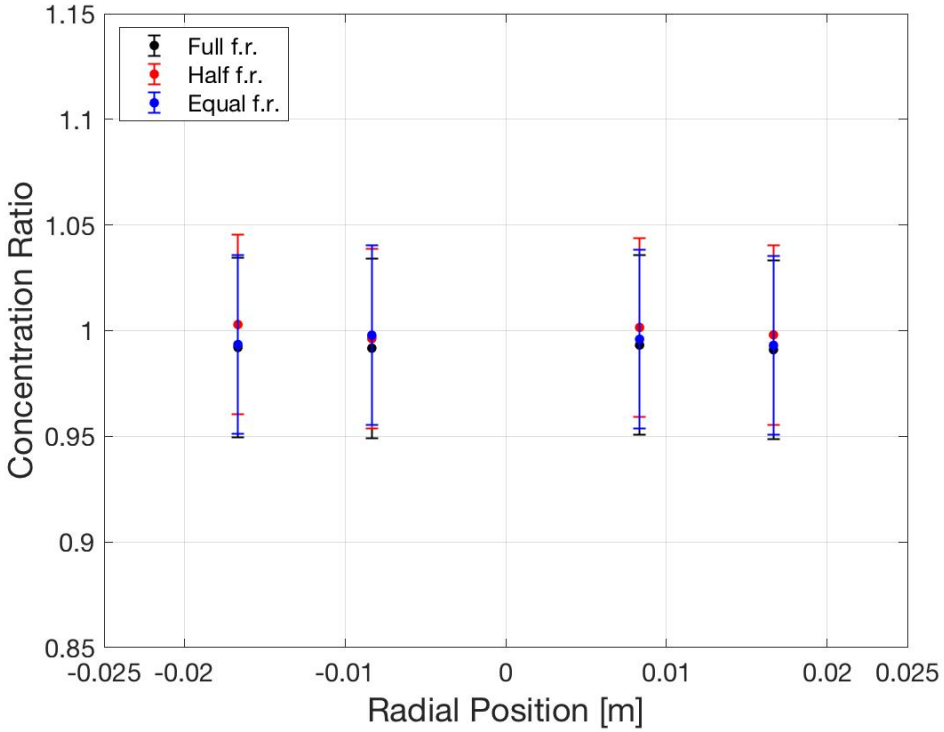

Figure 35: Short mixing chamber (0.57 m): normal, reduced and equal flow rates comparison using salt particles

In conclusion, the mixing quality of salt particles is achieved upstream 0.57 m, even with reduced flow rates. This is because of the small relaxation time of salt particles, which allows them to well exploit the turbulent flow.

The same procedure has been performed with an even shorter configuration of the mixing chamber, displaying only 0.35 m between the very top inlets and the sampling point. Results are shown in Figure 36.

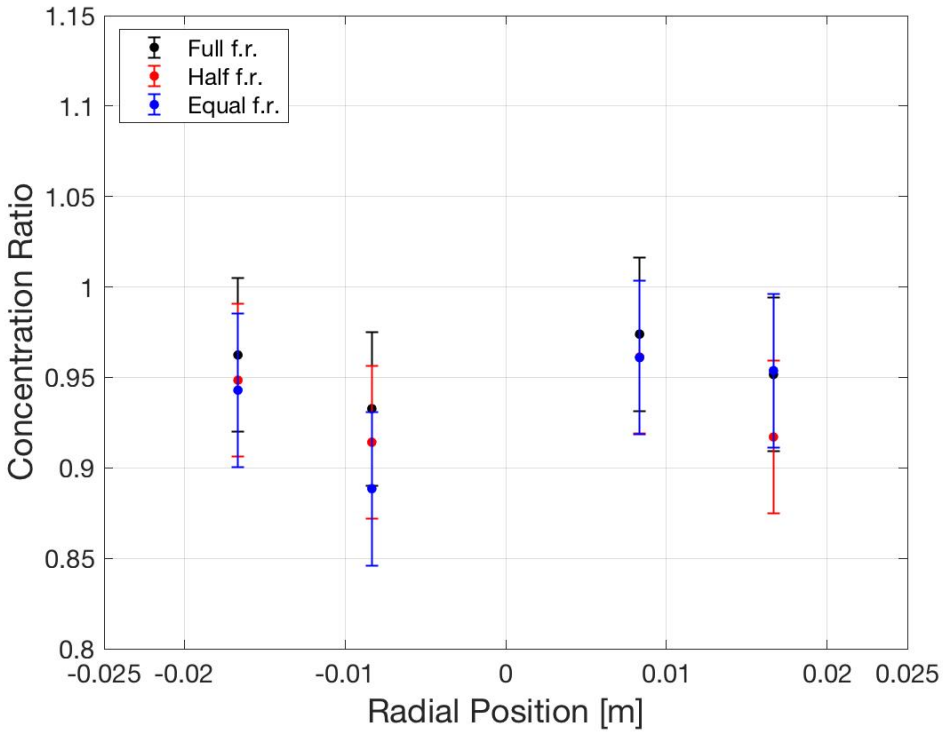

Figure 36: Shortest mixing chamber (0.35 m): normal, reduced and equal flow rates comparison using salt particles

The limit has been reached. Not even all the full flow measurements lie in the target interval. Conversely, all the half flow rates measurements and all but one of the equal flow rates measurements are out of it. High diffusivity and low relaxation time can do nothing to preserve the previous concentration homogeneity standards. Such a short chamber configuration is then *discarted*.

6 Discussion

6.1 Comparison of numerical and experimental results

To compare numerical and experimental results, outcomes of the *Transport of Diluted Species* model are picked. Instead, outcomes of the *Particle Tracing for Fluid Flows* are discarded. This is because of the few particles reaching the outlet of the mixing chamber, which do not allow a solid statistical analysis.

Figure 37 shows the comparison between the concentration ratios obtained experimentally and numerically. Data refer to z=0.70 m, the longest tested chamber.

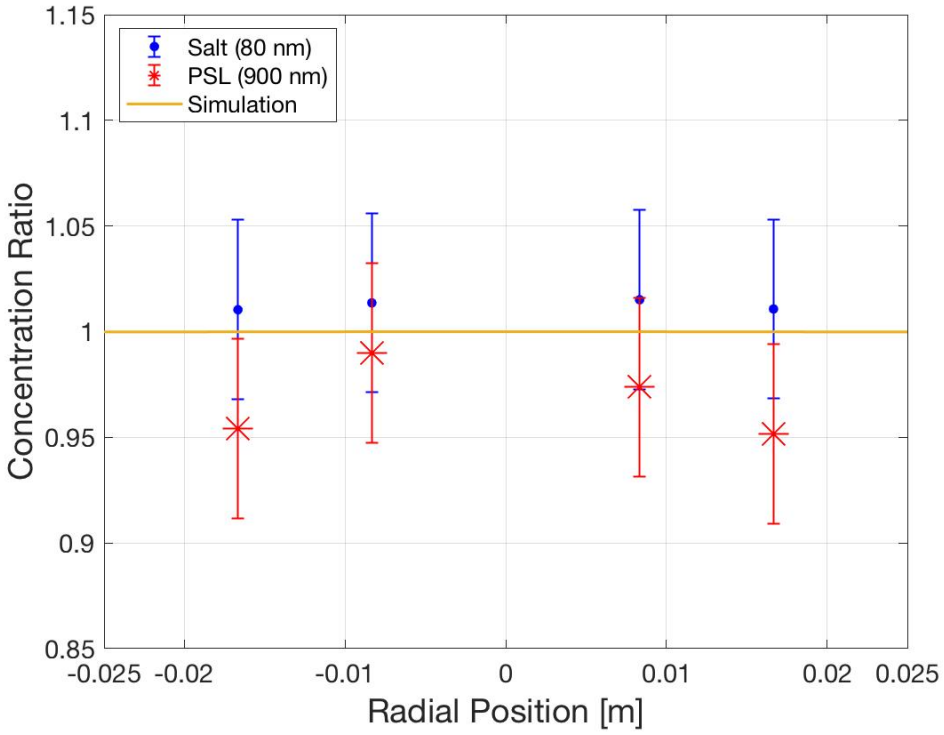

Figure 37: Flow rate reduction with salt particles: comparison

At a glance, one notices that simulations determine a much more homogeneous concentration than experiments. Moreover, the simulation curve lies

in between salt and PSL particle concentration ratios. As for salt particle measurements, the numerical outcome is included in the error bar of each ratio. As for PSL particle measurements, the numerical outcome is not included in the error bars of ratios close to the wall. Therefore, salt particle experiments *validate* the numerical simulation. Partial validation comes from the PSL particle measurements too. In addition, numerical data is always closer to the salt particle measurements than to PSL ones. The reason behind this lies in the diffusivity picked ($D = 10^{-10} m^2/s$) for the Transport of Diluted Species model. According to Einstein's relation (see equation 56) and to experimental findings shown in (*9*), the selected value corresponds to the diffusivity of particles with 100 nm diameter, thus close to NaCl particles (size peak at 80 nm) and almost one order of magnitude off the PSL particles diameter (size peak at 900 nm). On the other hand, one should not neglect that numerical results show an almost perfect concentration homogeneity. This is also the case far upstream the outlet, as shown in subsection 4.4. Simulations do not perfectly model what happens during experiments. For instance, the shape of the mixing chamber is slightly different from the virtual counterpart. Finally, the k-ε model may shift the position and change the dimension of vortexes, eventually increasing the convection.

7 Conclusion

Briefly, the aim of this project was to improve the performances of an aerosol mixing chamber, developing at its outlet the most homogeneous concentration as possible. Whether the dimensions and the flow rates of the chamber could be reduced without drastically affecting the concentration homogeneity has been investigated too.
To do so, CFD simulations in COMSOL Multyphysics have been run. The velocity field has been computed with a k-ε model and mixing mechanisms using a particle tracing and a diluted species model.
Finally, experiments using different particle size distributions ($NaCl$, size peak of 80 nm in diameter and PSL, size peak of 900 nm in diameter) and several mixing chamber configurations have been carried out.

7.1 What has been learnt

According to numerical simulations and experiments the mixing chamber delivers the target concentration homogeneity. This result has been confirmed with two particle size distributions, exploiting salt and Polystyrene Latex (PSL). The uncertainty on experimental measurements is of $\pm 4.24\%$ and is reasonable. Indeed, most of the error bars lie completely in the target range of the concentration ratio (0.95 - 1.05). This is always true in case of salt particles. Experiments show that salt particles always achieve higher concentration homogeneity than PSL particles. This is mainly due to their higher diffusivity ($D = 10^{-10} m^2/s$) and their smaller relaxation time ($\tau \approx 0.04 s$). In addition, salt particle experiments show that the flow rates in the mixing chamber can be halved (20 L/min from top and 10L/min from the sides) without compromising the concentration homogeneity, which still lies in the target range. Even lower and equal flow rates (10 L/min from top and 10L/min from the sides) are sufficient to achieve this goal. Both salt particle measurements and simulations show that the mixing chamber dimensions can be reduced to 0.57 m in length. In this case, half flow (20 L/min from top and 10L/min from the sides) and lower and equal (10 L/min from top and 10L/min from the sides) flow rates do not jeopardize the concentration homogeneity. When reducing the chamber dimension to 0.35 m in length, thus to the 50%, not even salt particles satisfy completely the concentration homogeneity target. In this case, flow rates cannot be reduced. As for numerical simulations, only the Transport of Diluted Species model

was successful. In COMSOL Multiphysics, particle tracing is not suitable to simulate the presented aerosol. However, the considered numerical computations have been validated by experiments. They overestimate what found during experiments, showing perfect concentration homogeneity at the outlet of the mixing chamber.

In conclusion, both experiments and numerical simulations tell that the mixing chamber can be used to provide the target concentration homogeneity, thus the main goal has been achieved. Furthermore, the mixing chamber can be used in its shorter configuration, at least for small particles, as confirmed by salt particle measurements and simulations. Therefore, the transportability goal has been achieved too.

8 Future Work

8.1 Possible Improvements

Future work involves both numerical simulations and experiments.
As for simulations, all those performed have to be tested on another software and results have to be compared. Suggested software are ANSYS Fluent and OpenFOAM. In this regard, it is fundamental to run a particle tracing model. If successful, its results can further enlighten about the mixing mechanisms taking place in the chamber. Moreover, simulations should vary the inclination of the slanted inlets, currently fixed at 30 deg. Other geometrical investigations should be performed, in order to see what shape contributes the most to the mixing.
As for the experiments, other particle size distribution can be tested, for instance over the micrometer. Moreover, the experimental procedure can be improved to reduce the measurement error. To do so, each sampling has to be taken three times, swapping the probes twice. Both of the CPCs would then measure each of the concentrations. During postprocessing calculations, this would allow to cancel out CPCs efficiencies and to reduce the uncertainty on each measurement.

Bibliography

1. R. Lantz *et al.*, *Society of Petroleum Engineers Journal* **11**, 315–320 (1971).
2. W. Jones, B. Launder, *Heat Mass Transfer* **15** (1972).
3. B. E. Launder, B. Sharma, *Letters in heat and mass transfer* **1**, 131–137 (1974).
4. R. D. Kimbrough, C. D. Carter, J. A. Liddle, R. E. Cline, P. E. Phillips, *Archives of Environmental Health: An International Journal* **32**, 77–86 (1977).
5. A. Gosman, E. Loannides, *Journal of energy* **7**, 482–490 (1983).
6. E. Treccani *et al.*, *Enciclopedia Italiana di scienze, lettere ed arti* (Roma, 1994).
7. D. G. Badman, E. R. Jaffé, *Otolaryngology–Head and Neck Surgery* **114**, 205–208 (1996).
8. S. Bottin, H. Chaté, *The European Physical Journal B-Condensed Matter and Complex Systems* **6**, 143–155 (1998).
9. W. C. Hinds, *Aerosol technology: properties, behavior, and measurement of airborne particles* (John Wiley & Sons, 1999).
10. S. Pope, *CFD Module, User's Guide* (Cambridge Univ. Press, 2000).
11. S. B. Riffat, S. Omer, *International Journal of Energy Research* **25**, 115–128 (2001).
12. M. Riediker *et al.*, *American journal of respiratory and critical care medicine* **169**, 934–940 (2004).
13. P. K. Mandal, *Journal of Comparative Physiology B* **175**, 221–230 (2005).
14. Y. Bartosiewicz, Z. Aidoun, Y. Mercadier, *Applied thermal engineering* **26**, 604–612 (2006).
15. J. Peixinho, T. Mullin, *Physical review letters* **96**, 094501 (2006).
16. T. Sriveerakul, S. Aphornratana, K. Chunnanond, *International Journal of Thermal Sciences* **46**, 812–822 (2007).
17. L. Tian, G. Ahmadi, *Journal of Aerosol Science* **38**, 377–397 (2007).
18. Y. Tominaga, T. Stathopoulos, *Atmospheric Environment* **41**, 8091–8099 (2007).

19. M. Kampa, E. Castanas, *Environmental pollution* **151**, 362–367 (2008).

20. S. Balachandar, J. K. Eaton, *Annual review of fluid mechanics* **42**, 111–133 (2010).

21. I. Colbeck, M. Lazaridis, *Naturwissenschaften* **97**, 117–131 (2010).

22. P. Kulkarni, P. A. Baron, K. Willeke, *Aerosol measurement: principles, techniques, and applications* (John Wiley & Sons, 2011).

23. H. Lomax, T. H. Pulliam, D. W. Zingg, *Fundamentals of computational fluid dynamics* (Springer Science & Business Media, 2013).

24. A. Petzold *et al.*, *Atmospheric Chemistry and Physics* **13**, 8365–8379 (2013).

25. N. Ruangtrakoon, T. Thongtip, S. Aphornratana, T. Sriveerakul, *International Journal of Thermal Sciences* **63**, 133–145 (2013).

26. H. Wu, Z. Liu, B. Han, Y. Li, *Desalination* **353**, 15–20 (2014).

27. R. Arina, *Fondamenti di Aerodinamica*.

28. W. Gao, D. Nelias, Y. Lyu, N. Boisson, *Tribology International* **123**, 43–49 (2018).

29. D. P. Karadimou, N.-C. Markatos, *Numerical Simulations in Engineering and Science*, 65 (2018).

30. M. Teti, M. Papini, J. K. Spelt, *The International Journal of Advanced Manufacturing Technology* **99**, 1283–1291 (2018).

31. S. Cândido, J. Páscoa Marques, A. Tomé, A. Amorim, S. K. Weber, presented at the ASME International Mechanical Engineering Congress and Exposition, vol. 59445, V007T08A065.

32. S. Horender, K. Auderset, K. Vasilatou, *Review of Scientific Instruments* **90**, 075111 (2019).

33. C. Multiphysics, *CFD Module, User's Guide*.

34. C. Multiphysics, *Particle Tracing Module, User's Guide*.

35. *AeroToX*, `http://empir.npl.co.uk/aerotox/`, Accessed: 10-06-2020.

36. *Condensation Particle Counters (CPC)*, `http://www.cas.manchester.ac.uk/restools/instruments/aerosol/cpc/`, Accessed: 15-07-2020.